Featuring work from the research groups of Wei Chen, National University of Singapore, Singapore and Zhenhua Ni, Southeast University, China.

Two-dimensional transition metal dichalcogenides: interface and defect engineering

This cover image illustrates the interface and defect engineering of two-dimensional TMDCs. Both methods could effectively modulate the electronic and optical properties of TMDCs, thus boosting the development of advanced (opto)electronic devices.

ROYAL SOCIETY OF CHEMISTRY

rsc.li/chem-soc-rev

REVIEW ARTICLE

Check for updates

Two-dimensional transition metal dichalcogenides: interface and defect engineering

Zehua Hu, †[abc] Zhangting Wu, †[d] Cheng Han, †[abe] Jun He, [f] Zhenhua Ni *[d] and Wei Chen *[abcg]

Two-dimensional (2D) transition metal dichalcogenides (TMDCs) have been considered as promising candidates for next generation nanoelectronics. Because of their atomically-thin structure and high surface to volume ratio, the interfaces involved in TMDC-based devices play a predominant role in determining the device performance, such as charge injection/collection at the metal/TMDC interface, and charge carrier trapping at the dielectric/TMDC interface. On the other hand, the crystalline structures of TMDCs are enriched by a variety of intrinsic defects, including vacancies, adatoms, grain boundaries, and substitutional impurities. Customized design and engineering of the interfaces and defects provides an effective way to modulate the properties of TMDCs and finally enhance the device performance. Herein, we summarize and highlight recent advances and state-of-the-art investigations on the interface and defect engineering of TMDCs and their corresponding applications in electronic and optoelectronic devices. Various interface engineering approaches for TMDCs are overviewed, including surface charge transfer doping, TMDC/metal contact engineering, and TMDC/dielectric interface engineering. Subsequently, different types of structural defects in TMDCs are introduced. Defect engineering strategies utilized to modulate the optical and electronic properties of TMDCs, as well as the developed high-performance and functional devices are summarized. Finally, we highlight the challenges and opportunities for interface and defect engineering in TMDC materials for electronics and optoelectronics.

[a] Department of Chemistry, National University of Singapore, 3 Science Drive 3, Singapore 117543, Singapore. E-mail: phycw@nus.edu.sg

[b] Centre for Advanced 2D Materials and Graphene Research Centre, National University of Singapore, 6 Science Drive 2, Singapore 117546, Singapore

[c] Department of Physics, National University of Singapore, 2 Science Drive 3, Singapore 117542, Singapore

[d] School of Physics, Southeast University, Nanjing 211189, China. E-mail: zhni@seu.edu.cn

[e] SZU-NUS Collaborative Innovation Center for Optoelectronic Science and Technology, Shenzhen University, Shenzhen 518060, China

[f] School of Physics and Electronics, Central South University, 932 South Lushan Road, Changsha, 410083, China

[g] National University of Singapore (Suzhou) Research Institute, 377 Lin Quan Street, Suzhou Industrial Park, Jiang Su 215123, China

† These authors contributed equally to this paper.

Mr Zehua Hu received his Bachelor's degree in physics from Nanjing University (China) in 2014. Currently, he is a PhD candidate in the National University of Singapore (NUS). His research interests include synthesis and characterization of novel 2D materials, and interface engineering of nanoscale optoelectronic devices.
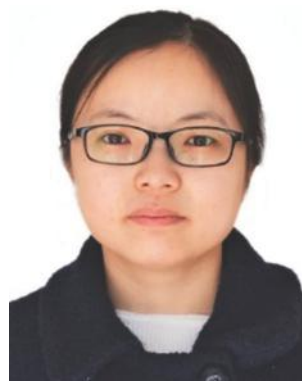
Zehua Hu

Dr Zhangting Wu received her PhD degree in Physics from Southeast University (China) in 2017. She is currently a lecturer in the College of Electronics and Information at Hangzhou Dianzi University (China). Her research interests include the spectroscopic investigation of defects and modulation of the properties of two-dimensional materials.

Zhangting Wu

3100 | *Chem. Soc. Rev.*, 2018, 47, 3100–3128

This journal is © The Royal Society of Chemistry 2018

1. Introduction

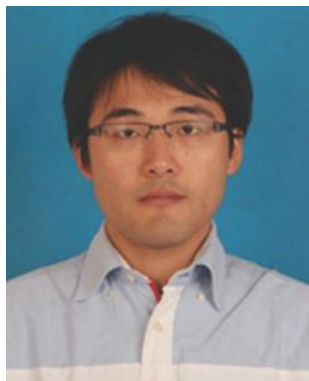Two-dimensional (2D) materials offer a new platform in both exploring fundamental physics and breaking through technological bottlenecks such as the scaling limit of bulk materials. Graphene, as the first discovered 2D material, has unique mechanical, thermal and electrical properties,[1] but the lack of a sizable energy gap limits its application in logic devices. Since then, a variety of 2D materials such as transition metal dichalcogenides (TMDCs),[2] black phosphorus (BP)[3] and hexagonal boron nitride (h-BN)[4] have been extensively investigated for their intriguing properties when thinned down to few- or even one-atomic layer. These fast-developing 2D materials, as well as their heterostructures, are now playing important roles in both fundamental research and technological applications.[5–11]

TMDCs are a class of materials with stoichiometry MX_2, where M is a transition metal of group IV, group V or group VI, and X represents a chalcogen. Due to the abundant atomic combinations and rich phases including 1T (trigonal symmetry), 2H (hexagonal symmetry) and 3R (rhombohedral symmetry), the TMDC family contains semiconductors (such as MoS_2, WSe_2), metals (such as 1T $MoTe_2$) and superconductors (such as NbS_2, $NbSe_2$), and therefore attracts intensive research attention. Among them, the most widely studied materials are 2H phase group VI TMDCs such as molybdenum disulfide (MoS_2) (Fig. 1a), with the calculated band structure shown in Fig. 1b.[12] The bandgap gradually increases from ~1.2 to ~1.9 eV when thinning down from bulk to a monolayer along with an indirect to direct bandgap cross-over. The unique electronic band structure enables a series of remarkable features, such as gate-tunable conductivity,[13] moderate mobility,[13] excellent photoresponse[6] and valley-selective optical excitation.[14,15] Based on these properties, different functional devices have been developed, including field-effect transistors (FETs),[13] broad-band photodetectors,[16] light-harvesting devices,[17] chemical sensors,[18] flexible devices[19] and valleytronics,[14,15] and so on.

Unlike the bulk materials, atomic-thin 2D materials are essentially interface-type materials and the performance of their devices is controlled and determined by the interface.[20,21] In a typical TMDC-based FET device, three types of interfaces are usually involved, including (i) TMDC/adsorbate, (ii) TMDC/metal contact, and (iii) TMDC/dielectric interfaces, as indicated in Fig. 1c. The effective control of the properties of these interface offers the opportunity to optimize the device performance as well as to realize devices with novel functionalities. For example, the surface adsorbates can effectively and non-destructively dope the TMDCs to obtain a desired carrier type and concentration;[22] the charge carrier transport in TMDCs is dominated by the contact between the TMDCs and electrodes[23] as well as the scattering at the dielectric interfaces.[13] This results in a great necessity to understand and utilize interface engineering to achieve high-performance TMDC-based devices.[25,26]

On the other hand, the crystals of TMDCs are enriched by a variety of intrinsic defects, such as vacancies, adatoms, grain boundaries, and substitutional impurities, as shown in Fig. 1d. The presence of these defects leads to a significant impact on

Dr Cheng Han is currently an assistant professor of Shenzhen University (SZU, China). He received his Bachelor's degree in Physics from Sichuan University (SCU, China) in 2009 and his PhD degree in Physics from the National University of Singapore (NUS, Singapore) in 2014. He did research as a postdoctoral fellow in the Chemistry Department, the National University of Singapore from 2014 to 2017. His research interests mainly focus on the interface engineering of novel material-based functional devices, especially for low-dimensional materials.

Cheng Han

Dr Zhenhua Ni is currently a professor in the School of Physics at Southeast University (SEU, China). He received his Bachelor's degree in Physics from Shanghai Jiaotong University (SJTU, China) in 2003, PhD degree in Physics from the National University of Singapore (NUS, Singapore) in 2007, and did his postdoctoral research in the Department of Physics and Applied Physics at Nanyang Technological University (NTU, Singapore) from 2007–2010. His current research interests include the spectroscopic investigation of two dimensional materials and their applications in optoelectronic devices, e.g. phtotodetectors.

Zhenhua Ni

Dr Wei Chen is currently an Associate Professor in both the Chemistry Department and Physics Department at the National University of Singapore (NUS). He received his Bachelor's degree in Chemistry from Nanjing University (China) in 2001 and PhD degree from the Chemistry Department at NUS in 2004. His current research interests include molecular-scale interface engineering for organic and 2D material-based optoelectronics, and interface-controlled nanocatalysis for energy and environmental research.
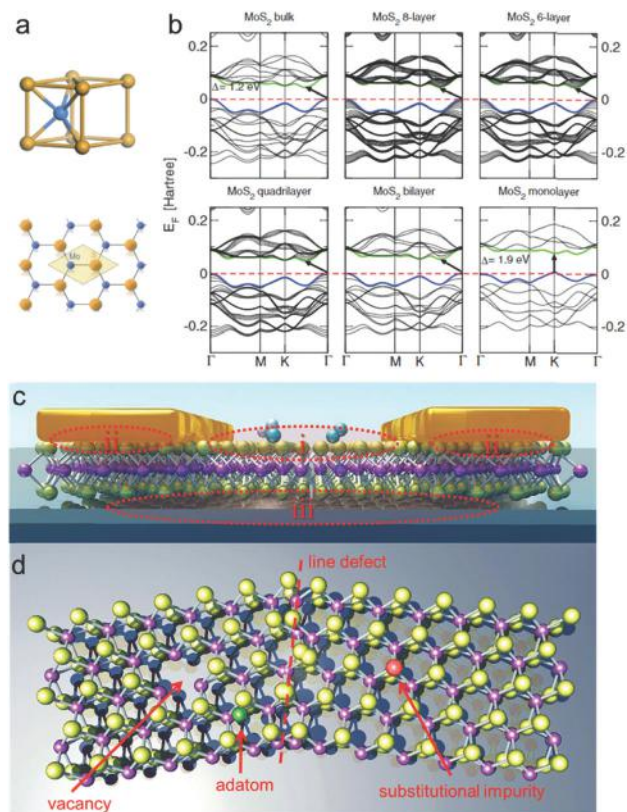
Wei Chen

This journal is © The Royal Society of Chemistry 2018

Chem. Soc. Rev., 2018, **47**, 3100–3128 | 3101

Fig. 1 (a) Unit cell (top) and top view (bottom) of the 2H-MoS$_2$ lattice. (b) Calculated band structure of MoS$_2$ with a decreasing number of layers, indicating a transition from an indirect to a direct band gap. (c) Schematic illustration of the three interfaces in a TMDC-based FET device, including the TMDC/surface adsorbate, TMDC/metal contact and TMDC/dielectric interface, which are highlighted by the dashed circles. (d) Schematic of the MoS$_2$ crystal structure with typical defects, including vacancy, adatom, substitutional impurity and line defects. Reprinted with permission from: (a) ref. 24, Copyright 2012, Nature Publishing Group; (b) ref. 12, Copyright 2011, American Physical Society.

the optical and electronic properties of TMDCs,[27–34] making it crucial to develop various strategies of defect engineering for the realization of materials with novel features as well as high-performance devices. The rational design of defects is able to facilitate carrier transport, induce effective doping and modulate the band[35,36] and phase structures[37] in TMDCs, based on which multifunctional heterostructures or devices can be constructed. Therefore, understanding the role of defects as well as developing effective defect engineering schemes is of great significance for the future development of TMDC-based electronics and optoelectronics.

In this review, we summarize the recent progress and development in understanding the effects of interfaces and defects on TMDCs for electronics and optoelectronics. In the first part on interface engineering, we start from surface charge transfer doping (SCTD) at the TMDC/adsorbate interface and discuss its impact on the electronic and optical properties of TMDCs, as well as practical applications in electronic and optoelectronic devices. Subsequently, the interface at the TMDC/metal contact will be introduced by providing several strategies of contact engineering

to improve the device performance. This part ends with a discussion on the TMDC/dielectric interface. Notably, other than traditional high-k dielectrics, a detailed review will be given on a family of fast-emerging dielectric materials, *i.e.* ferroelectric films, which bring intriguing functionalities. In the second part on defect engineering, we will first provide a brief overview of the existing defects in TMDCs, including vacancies, substitutional impurities, line defects and local phase transition, as well as their effects on electronic and optical properties. We then discuss how defect engineering is able to modulate the optical and electronic properties and create materials and devices with novel functionalities, *e.g.* photoconductors, photovoltaics, and quantum light emitting diodes (LEDs). Finally, a summary and outlook are given towards the future development of interface and defect engineering on TMDCs.

2. Interface engineering of TMDCs and its application in electronic and optoelectronic devices

2.1. Surface charge transfer doping

Fast development of 2D TMDCs has led to high demand for expanding their applications in electronic and optoelectronic devices as well as optimizing the device performance. In particular, it is crucial to control the charge carrier type and concentration in TMDCs. SCTD, as a strong and non-destructive doping methodology, relies on the interfacial charge transfer between the surface dopant and underlying semiconductor.[38] This process is driven by the energy level alignment at the interfaces (*i.e.* adsorbate/semiconductor, semiconductor/semiconductor, oxide/semiconductor, or metal/semiconductor interface), in particular the misalignment of Fermi levels, which has been systematically investigated in conventional solid-state physics.[39] Unlike the traditional substitutional doping or plasma treatment, SCTD does not introduce significant amounts of defects or destroy the crystal structure of the underlying semiconductors, and is thereby known as a defect-free doping scheme. Compared with the electrostatic modulation *via* an external electrical field, SCTD usually provides a stronger and non-volatile doping capability with ease of device fabrication. In the pioneering studies, SCTD was used to tune the conductivity of carbon-based materials such as graphene, diamond[38,40–45] and organic semiconductors.[46–49] Recently, this doping strategy has been applied to a variety of 2D materials including TMDCs,[9,10,50] BP[42,51–54] *etc.* In the following sections, we will illustrate the mechanism of SCTD and summarize its effects on the modulation of the electronic and optical properties of TMDCs.

2.1.1. SCTD mechanism. The mechanism of SCTD on TMDCs can be schematically illustrated by the band/energy level diagrams in Fig. 2. Here we use the SCTD process between organic molecules and MoS$_2$, the most studied TMDC, as an example to show the underlying mechanism, which is also applicable to other dopant/semiconductor systems. The electron affinity (EA, termed as χ) and ionization potential (IP) of the adsorbed molecules are two key parameters to determine the charge transfer at the

3102 | *Chem. Soc. Rev.*, 2018, **47**, 3100–3128

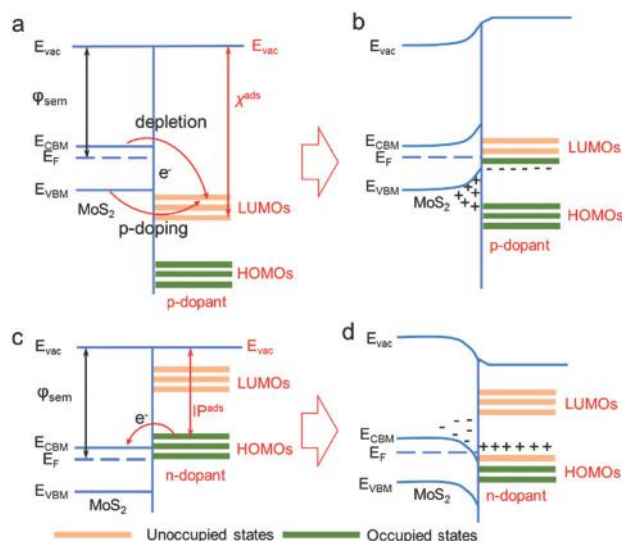This journal is © The Royal Society of Chemistry 2018

Fig. 2 Schematic energy level diagrams of SCTD between organic molecules and MoS₂. (a and b) Depletion and p-doping process *via* SCTD of organic molecules with high EA; (c and d) n-doping on MoS₂ *via* SCTD of organic molecules with low IP.

molecule/MoS₂ interface, where EA or IP refers to the energy difference between the vacuum level and lowest unoccupied molecular orbital (LUMO) or highest occupied molecular orbital (HOMO), respectively. For the molecules with high EA and their LUMO locating below the VBM of MoS₂ [*e.g.* 2,3,5,6-tetrafluoro-7,7,8,8-tetracyanoquinodimethane (F₄TCNQ)[55]], the electrons will be spontaneously transferred from MoS₂ to the LUMO of the molecules, as exhibited in Fig. 2a. This results in hole accumulation or p-type doping in MoS₂, and hence the upward band bending of MoS₂ at the molecule/MoS₂ interface (Fig. 2b). In contrast, for the molecules with low IP and their HOMO lying above the CBM of MoS₂ (*e.g.* benzyl viologen[56]), spontaneous electron transfer will occur from the HOMO of the molecules to MoS₂, thus resulting in an n-type doping on MoS₂ and its downward band bending (Fig. 2c and d). The injected charge carriers induced by such a process can be confined at the MoS₂/molecule interface and continuously contribute to the charge transport in MoS₂.[38] For the SCTD occurring between TMDCs and other surface dopants, such as metals and metal-oxides, the work function (WF) of the dopants should be used for comparison instead of EA and IP in organic molecules. Consequently, SCTD is able to effectively modulate the charge carrier type and concentration in TMDCs, and thereby impose deep impacts on both the electronic and optical properties of TMDCs.

2.1.2. The modulation of electronic properties. Recently, a large variety of chemical dopants have been utilized to tune the electronic properties of 2D TMDCs, among which benzyl viologen (BV),[56] potassium (K),[57] cesium carbonate (Cs₂CO₃),[58,59] triphenylphosphine (PPH₃),[60] nicotinamide adenine dinucleotide (NaDH),[55] ammonia (NH₃),[61] chloride molecular,[62] DNA,[63] dehydrated poly(vinyl-alcohol) (PVA),[64] polyethyleneimine (PEI)[65] tetrathiafulvalene (TTF),[66] acetone and triethylamine (TEA)[18] serve as n-dopants; while AuCl₃,[25,67,68] O₂/H₂O,[69] molybdenum trioxide

(MoO₃),[70] 7,7,8,8-tetracyanoquinodimethane (TCNQ), F₄TCNQ,[55] nitrogen oxide (NOₓ),[61,71] bis(trifluoromethane) sulfonimide (TFSI),[72] octyltrichlorosilane (OTS),[73] and metal ion modified DNA[63] serve as p-dopants. Of these species, K,[57] BV,[56] and NOₓ[61,71] exhibit an extremely strong electron donating or accepting capability that can shift the Fermi level of TMDCs even above the CBM or below the VBM, respectively, corresponding to a degenerate doping process (Fig. 2d). As an organic compound with a high electron reduction potential (*i.e.* low IP), BV possesses a great electron donating behavior.[74,75] Upon physical contact with MoS₂, it can significantly increase the electron density of MoS₂ to a remarkably high level of ~1.2 × 10¹³ cm⁻², but unfortunately this decreases its on/off ratio to less than 10. Furthermore, a BV-doped MoS₂ device shows a superior stability in air ambient and the BV layer can be simply removed by rinsing in toluene solution. As a comparison, the non-degenerate n-dopant, Cs₂CO₃,[58,59] can effectively increase the electron concentration of MoS₂ and WSe₂ by almost one order of magnitude, while retaining good semiconducting properties like high on/off ratio and gate tunability. Owing to the filling and screening of charge trapping sites by the increased electron concentration, the electron mobility of MoS₂ and WSe₂ can be enhanced by ~3 and 5 times, respectively.[58,59] On the other hand, the typical degenerate p-dopant, NO₂, is able to shift the Fermi level of WSe₂ below the VBM,[71] revealing its strong electron accepting behaviour. However, this doping scheme suffers from its volatile nature due to the weak adsorption strength of NO₂ on TMDCs,[61] which can be solved by a chemical reaction at 150 °C[76] to form chemisorbed NO₂. The most widely used non-degenerate p-type dopant is AuCl₃,[25,67,68] which can draw electrons from TMDCs and then be chemically reduced to Au nanoparticles, leading to the p-doping of TMDC devices. AuCl₃-based SCTD can be easily achieved *via* a standard solution-based process and thus has been extensively used to p-dope MoS₂,[67] and WSe₂,[68] as well as integrated into functional (opto)electronic devices.[25]

2.1.3. The modulation of optical properties. Owing to the strong electron–phonon interaction in 2D systems, the charge carrier concentration of 2D materials can greatly affect the phonon frequencies,[77] which can be characterized by Raman spectroscopy. Raman spectra of few layer MoS₂ before and after SCTD induced n- (DNA) and p-doping (metal ion-modified DNA) are presented in Fig. 3a and b. For MoS₂ n-doped by DNA, both vibration modes of E_{2g}^1 and A_{1g} are red-shifted by 1.9–2.3 cm⁻¹ and 1.8–2.0 cm⁻¹, respectively; while for MoS₂ p-doped by metal ion-modified DNA, E_{2g}^1 and A_{1g} are blue-shifted, with the wavenumbers determined by the metal-ions (Fig. 3b).[63] Similar phenomena were also revealed on other TMDCs such as WSe₂[68] and other dopants like BV[56] and Cs₂CO₃.[58,59] Therefore, Raman spectroscopy is considered to be an effective technique to characterize the doping process in TMDCs.

In addition to the Raman spectra, the photoluminescence (PL) spectra of TMDCs also strongly depend on the doping level. Upon light illumination, the photo-induced excitons (X⁰) in TMDCs are tightly bound due to the quantum confinement effect and reduced dielectric screening in 2D TMDCs. They can further interact with free charge carriers (h⁺/e⁻) and
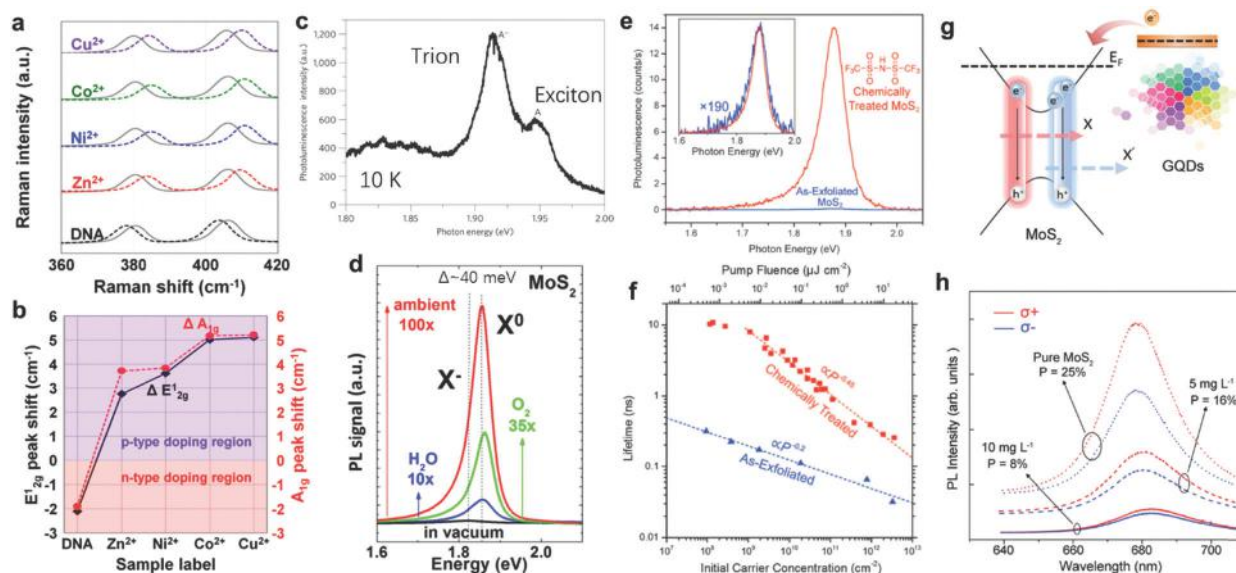
This journal is © The Royal Society of Chemistry 2018

Chem. Soc. Rev., 2018, **47**, 3100–3128 | 3103

Fig. 3 (a) Raman spectra of MoS_2 doped by DNA or metal ion-modified DNA, and (b) extracted E^1_{2g} and A_{1g} peak shift data for MoS_2. (c) PL spectrum of a monolayer of MoS_2 on a h-BN substrate at 10 K. (d) Comparison of the PL spectra of monolayer MoS_2 under vacuum and upon exposure to H_2O, O_2, and ambient air, respectively. (e) PL spectrum of both as-exfoliated and TFSI-treated MoS_2 monolayers. (f) Effective PL lifetime as a function of pump fluence. (g) Schematic of the formation of the exciton and trion as well as the charge transfer occurring in GQD-doped MoS_2. (h) Circularly polarized PL spectra and the degree of circular polarization (P) of the pure MoS_2 and GQD/MoS_2 heterostructures with different GQD concentrations. Reprinted with permission from: (a and b) ref. 63, Copyright 2014, American Chemical Society; (c) ref. 15, Copyright 2012, Nature Publishing Group; (d) ref. 69, Copyright 2013, American Chemical Society; (e and f) ref. 72, Copyright 2015, American Association for the Advancement of Science. (g and h) Ref. 78, Copyright 2015, John Wiley and Sons.

form charged exctions (termed as trions). The formation of positive/negative trions (X^+/X^-) needs extra binding energies ($E_{b1} = E(X^0) - E(X^{+/-})$) to bind the free carriers, resulting in the lower emission energy of a trion than the corresponding exciton. As illustrated in Fig. 3c, the low temperature PL spectrum clearly resolves the trion and exciton emission peaks for monolayer MoS_2 on an h-BN substrate, with an energy difference (trion binding energy) between these two peaks of ~ 34 meV. Compared with the electrostatic modulation on trion states via an external electrical field,[79,80] SCTD provides a stronger and easy-access doping strategy to tune the carrier concentration and hence the PL emission of TMDCs.

O_2 and H_2O molecules in air can physisorb on the surface of MoS_2, thus depleting the free electrons in the intrinsically n-doped MoS_2. Such electron depletion converts the PL emission process from X^- to X^0 and also suppresses the electrostatic screening effect and nonradiative recombination, thereby greatly enhancing the quantum yield. As a result, the PL intensity of monolayer MoS_2 is remarkably increased by over 100 times along with a 40 meV blue shift (Fig. 3d).[69] Similar PL enhancement under air exposure is also observed in other n-type TMDCs like $MoSe_2$, but is reversed in p-type WSe_2 (PL intensity is further suppressed after exposure to O_2 and H_2O).[69] Following this report, Mouri et al. modulated the PL characteristics of monolayer MoS_2 via a solution-based SCTD process.[55] The PL intensity is enhanced by over 10 times using p-dopant TCNQ/F4TCNQ, but reduced by using electron donor, NADH.[55] Amani et al. achieved a uniformly-enhanced PL intensity in monolayer MoS_2 by more than two orders of magnitude via an organic superacid

bis(trifluoro-methane) sulfonimide (TFSI) treatment (Fig. 3e),[72] reaching $\sim 95\%$ quantum yield. The TFSI treatment can help deplete the extra electrons as well as eliminate the defects in MoS_2. By performing time-resolved PL measurement, it was found that the exciton lifetime is largely enhanced after the treatment. At the lowest measurable pump fluence of 5×10^{-4} μJ, the treated sample features a lifetime of $\sim 10.8 \pm 0.6$ ns, compared to the lifetime of ~ 0.3 ns in the pristine MoS_2 (Fig. 3f).[72]

Light excitation can also lead to SCTD in heterostructures and further tune the optical properties of TMDCs. In a graphene quantum dot (GQD)/MoS_2 heterostructure, photo-generated electrons transfer from the HOMO of GQDs to the CB of MoS_2 (Fig. 3g).[78] In addition to the suppressed PL intensity, the valley polarization of MoS_2 can also be tuned by such SCTD processes, as shown in Fig. 3f. The degree of circular polarization (P) is defined as $P = (I^+ - I^-)/(I^+ + I^-)$, where I^+ and I^- represent the PL intensity of right handed σ^+ and left handed σ^- circularly polarized light, respectively. At a high doping level, P decreases from 25% (pure MoS_2) to 8% (10 mg ml^{-1} GQDs on MoS_2), as shown in Fig. 3h.[78] The valley depolarization at a high doping level can be ascribed to the enhanced electron–electron interaction. Electron spins tend to be inversed under inter-collision, leading to conversion from a bright to a dark exciton or nonradiative dissipation.[81]

2.1.4. Application of SCTD in electronic and optoelectronic devices. Based on the strong tunability of the electronic and optical properties of TMDCs, SCTD can be applied to improve the performance of TMDC-based electronic and optoelectronic devices. In a pioneering work, Lin et al. utilized Cs_2CO_3 to

3104 | Chem. Soc. Rev., 2018, 47, 3100–3128

This journal is © The Royal Society of Chemistry 2018

achieve effective n-doping of an MoS_2 FET.[58] The excess electrons injected by Cs_2CO_3 can tightly bind with excitons to form X^- in monolayer MoS_2, which prolongs the lifetime of the photo-induced excitonic state, and hence enhances the photoresponsivity by ~ 5 times (Fig. 4a–c). In addition, Cs_2CO_3 has been also utilized to n-dope WSe_2, resulting in a dramatic photocurrent increase by nearly three orders of magnitude.[59] Such enhancement of the device performance is attributed to the reduction of the contact resistance and the decrease of the recombination probability of photo-excited excitons. Organic n-type dopant, PPh_3, consisting of lone pairs of phosphorus atoms, can dramatically enhance the photoresponsivity of WSe_2 from 2.7×10^3 to 4.3×10^5 only with a fractional deterioration of response speed.[60] Self-assembled monolayers (SAMs) are another family of effective dopants for TMDCs. For example, a p-doped WSe_2 phototransistor decorated by octadecyltrichlorosilane (OTS) achieves great enhancement of both field-effect mobility (by 5 times), photoresponsivity (by 28 times) and detectivity (by 26 times); while a comparable enhancement can be achieved in n-doped MoS_2 by coating with 3-aminopropyltriethoxysilane (APTES) SAM.[82]

Using a spatially controlled doping scheme to establish a p–n junction is another strategy to realize TMDC-based functional devices. A typical schematic drawing of the junction structure is shown in Fig. 4d, where the MoS_2 device is constructed with asymmetric electrodes (Pd, Cr/Au) to facilitate the carrier transport at each side.[25] Half of the channel was masked by h-BN while the other half was p-doped by $AuCl_3$ solution, thereby forming a p–n diode across the two regimes. The p–n junction possesses an ideal diode behavior with an ideal factor $n = 1$, as revealed by the I–V characteristic in Fig. 4e. Furthermore, the diode device shows an excellent photodetecting performance with a responsivity of ~ 5 A W^{-1} and an external quantum efficiency (EQE) of $\sim 1200\%$ at $V_D = 1.5$ V. In addition, an apparent open circuit voltage (V_{oc}) and short circuit current (I_{sc}) are observed upon illumination, revealing a photovoltaic characteristic. The built-in potential across the junction can effectively separate the photo-generated electron–hole pairs, resulting in a solar cell device with wide spectrum response (350–700 nm, Fig. 4f). Although the above lateral homojunction demonstrates a near 'ideal' diode performance, the active junction area for light absorption is relatively small. Further optimization
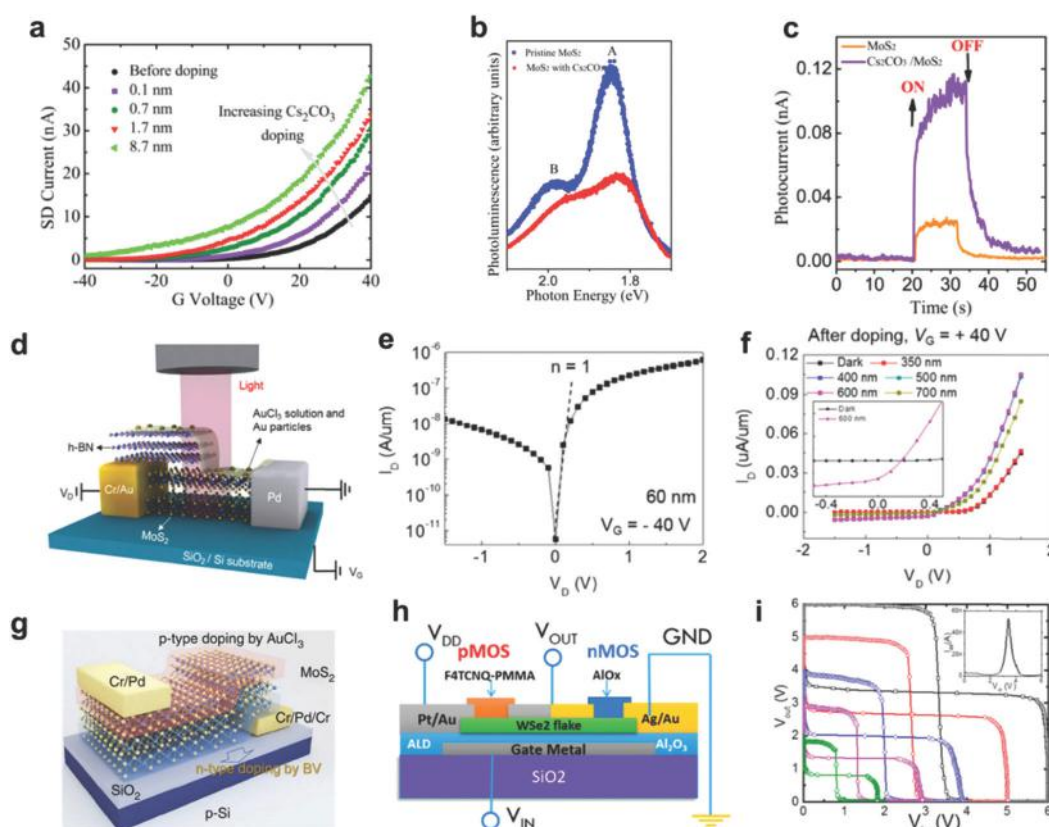

Fig. 4 (a) Transfer characteristics of the MoS_2 FET under vacuum with increasing Cs_2CO_3 thickness ($V_{ds} = 100$ mV). (b) PL spectra of 1L-MoS_2 before and after Cs_2CO_3 (0.7 nm) doping. (c) Photocurrent of the device without and with Cs_2CO_3 decoration, respectively ($V_{ds} = 20$ mV, $V_g = 0$ V). (d) Schematic diagram of the MoS_2 p–n diodes with $AuCl_3$ doping under light illumination. (e) I–V curves of the MoS_2 diode at $V_g = 40$ V with the ideal factor of $n = 1$. (f) Photovoltaic behavior of the doping-induced p–n junction upon light illumination with different wavelengths. Inset shows the enlarged I–V diagram curve under 600 nm light irradiation. (g) Schematic drawing of the vertical p–n junction in MoS_2. (h) Schematic image of the device structure for a WSe_2 inverter. (i) The output signal ($V_{out} - V_{in}$) of the WSe_2 inverter with V_{dd} ranging from 2 to 6 V. Inset: The channel current versus the input voltage. Reprinted with permission from: (a–c) ref. 58, Copyright 2014, American Chemical Society; (d–f) ref. 25, Copyright 2014, American Chemical Society; (g) ref. 86, Copyright 2015, Nature Publishing Group; (h and i) ref. 26, Copyright 2015, American Chemical Society.

This journal is © The Royal Society of Chemistry 2018

Chem. Soc. Rev., 2018, 47, 3100–3128 | 3105

can be realized by building up a vertical p–n junction to obtain a much larger planar active area. A widely adopted method is to stack 2D materials with different polarities together to achieve 2D–2D heterojunctions, which has attracted intensive research efforts in the last few years.[10,83–85] Another possible solution with easy-access and high-productivity is to obtain a vertical homojunction. As shown in Fig. 4g, after a 4-step fabrication process, BV and $AuCl_3$ were used to dope two sides of MoS_2 in the opposite manner to build up a vertical p–n junction. The fabricated device shows a high photocurrent on/off ratio of ~ 100 under 655 nm light illumination. Meanwhile, the photovoltaic performance such as power-conversion efficiency, fill factor and photoresponsivity were estimated to be 0.4%, 0.22 and 30 mA W^{-1} under standard solar simulator illumination.[86]

SCTD has also been widely implemented in TMDCs to construct complementary logic devices, such as a logic inverter.[26,87,88] A WSe_2-based inverter consists of two separated nMOS and pMOS FET channels in parallel, with low (Ag) and high (Pt) WF metal contacts, respectively.[26] The nMOS channel was protected by an AlO_x layer prior to the treatment by F_4TCNQ-poly (methyl methacrylate) (PMMA) on the pMOS channel, as shown in Fig. 4h. Upon supplying a voltage (V_{dd}) from 2 to 6 V, the device shows an excellent signal inversion performance, such as full logic swing, fast transition, symmetrical shape, high noise margin and almost zero current under 0 V voltage (Fig. 4i). The gain of the inverter, defined as the slope dV_{out}/dV_{in} of the output characteristic, is calculated to be as high as ~ 38. Meanwhile, the static power, defined as $P_{static} = V_{dd}(I_{static\_low} + I_{static\_high})/2$, is as low as 2 pW at $V_{dd} = 2$ V. In a similar device configuration, a $MoTe_2$-based inverter was fabricated by atomic layer deposition (ALD) induced hydrogen diffusion, achieving a DC voltage gain of 29 and an AC gain of 18 at 1 kHz,[87] respectively.

2.2. TMDC/metal contact engineering.

To improve the device performance of TMDCs, it is crucial to optimize the electrical contact.[89–95] The large bandgap of TMDCs leads to a Schottky barrier (SB) at the metal electrode/TMDC interface, resulting in a high contact resistance for the as-fabricated devices. Furthermore, an SB may still exist even using a contact metal with matched WF due to the Fermi level pinning effect.[91]

Contact engineering is a promising approach to lower the SB at the metal/TMDC interface and eventually enhance the device performance. For example, both n- and p-type behavior can be realized in the same TMDCs via suitable contact engineering. The representative contact engineering strategies include the selection of suitable metal contact, metal contact doping and buffer layer engineering strategies.

2.2.1. Selection of a suitable metal contact. A number of metal materials, such as aluminium (Al), tungsten (W), gold (Au), platinum (Pt), scandium (Sc), titanium (Ti) and nickel (Ni) have been applied in contact with TMDCs to optimize the device performance.[89–93,96–101] For n-type MoS_2, metals with low WF are found to form low SBs for electrons with MoS_2, thereby facilitating the electron transport in MoS_2 FETs. For example, Sc (WF = 3.5 eV) and Ti (WF = 4.3 eV) contacted MoS_2 devices show a small SB
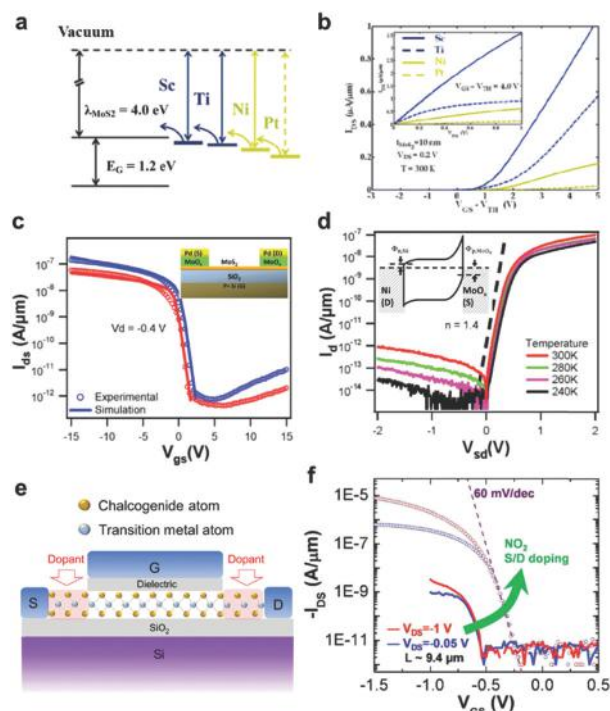

Fig. 5 (a) Line-up of the Fermi level of different metals with respect to the band structure of MoS_2 based on the experimental data. (b) Transfer characteristics of MoS_2 FETs with Sc, Ti, Ni, and Pt metal contacts at $V_{DS} = 0.2$ V. The inset shows the output characteristics of the corresponding devices for a gate voltage overdrive of 4.0–5.0 V. (c) $I_{ds}-V_{gs}$ characteristics of a MoS_2 pFET with MoO_x contacts. Inset shows the device structure. (d) Temperature-dependent $I-V$ curve of the diode with asymmetric Ni and MoO_3 electrodes. Inset: Qualitative band structure of the device. (e) Schematic drawing of a horizontally contact-doped TMDC device. (f) Transfer characteristics of a WSe_2 device before and after NO_2 contact doping. Reprinted with permission from: (a and b) ref. 91, Copyright 2012, American Chemical Society; (c and d) ref. 107, Copyright 2014, American Chemical Society; (f) ref. 71, Copyright 2012, American Chemical Society.

height (φ_B) of ~ 30 meV and ~ 50 meV, respectively (Fig. 5a and b).[91] In particular, Sc-contacted few-layer MoS_2 achieves a high field-effect mobility of ~ 184 cm^2 V^{-1} s^{-1}, and this could be further improved to ~ 700 cm^2 V^{-1} s^{-1} by coating with an Al_2O_3 layer. On the other hand, the deposited metal interacts strongly with the top S atoms through metal–S hybridization, which in turn weakens the lattice Mo–S bonding, and thereby induces surface states of Mo d-orbitals within the bandgap.[102] This leads to the strong Fermi level pinning effect in MoS_2 for most of the metal contacts, even when a high WF material like Pd has been used (Fig. 5a).[91] This effect was extensively investigated in metal-contacted MoS_2 devices, but seems not so obvious for other TMDCs. For example, both n- and p-type transport can be realized in WSe_2-based FETs with the selection of suitable metal contacts.[93,103,104] By using high WF metal Au as a contact, a sizable SB exists at the MoS_2/Au interface,[91,105] but the 'Ohmic performance' can still be observed in a low bias region.[13,106] Meanwhile, Au tends to form clusters or even nanostructures on MoS_2 surfaces, thus restricting the electron injection and producing overheating at the contact regions.[93]

3106 | Chem. Soc. Rev., 2018, 47, 3100–3128

This journal is © The Royal Society of Chemistry 2018

2.2.2. Contact doping. Recently, Steven *et al.* realized efficient hole injection in few-layer MoS$_2$ FETs by selectively p-type doping the contact area of MoS$_2$ beneath the electrodes using high WF material MoO$_x$, as shown in the inset of Fig. 5c.[107] The introduction of a MoO$_x$ interlayer effectively suppresses the Fermi-level pinning effect between MoS$_2$ and the metal electrodes, thus enabling p-type conduction in MoS$_2$. MoS$_2$ Schottky diodes with rectification ratio $\sim 10^6$ can be achieved by using asymmetric contacts (Fig. 5d, Ni as electron contact and MoO$_x$/Pd as a hole contact).[107] Yang *et al.* achieved effective chloride molecular doping by immersion of WS$_2$ and MoS$_2$ flakes into undiluted 1,2-dichloroethane (DCE). The contact resistance of WS$_2$–Ni and MoS$_2$–Ni after treatment can be reduced by 2–3 orders of magnitude to 0.7 and 0.5 kΩ μm, respectively.[62]

Horizontal contact doping, defined as doping the channel region in the proximity of the metal contact (Fig. 5e), can also lower the SB at the TMDC/metal interface, thereby facilitating efficient carrier injection into the conduction channel. Recently, Javey's group adopted this doping scheme on MoS$_2$ and WSe$_2$ FETs to optimize the device performance by using NO$_2$ (Fig. 5f)[71] and K[57] as degenerate hole and electron dopants, respectively. WSe$_2$ FETs with NO$_2$ doped contacts exhibit an excellent hole field-effect mobility of ~ 250 cm^2 V^{-1} s^{-1}, near ideal subthreshold swing of ~ 60 mV dec^{-1} and high I_{on}/I_{off} larger than 10^6; while K-contact-doped WSe$_2$ shows a high electron field-effect mobility up to ~ 100 cm^2 V^{-1} s^{-1}. The K-contact-doped nFET was then integrated with a Pd contacted pFET on the same flake to demonstrate a logic inverter with a high gain of ~ 13.[108] However, NO$_2$ or K doped devices suffer from poor air stability due to the high chemical reactivity of the surface dopant, which can be solved by using stable dopants such as BV[56] and AuCl$_3$.[88]

Another interesting contact doping method is to utilize a layer of photoresist such as hydrogen silsesquioxane (HSQ)[109] and cross-linked PMMA[110] as a dopant. Perera *et al.* selectively covered the MoS$_2$ contact and the vicinity of the channel area with HSQ and then used low beam dosages to destroy the Si–H bond in HSQ and release hydrogens to induce n-doping on the contact.[109] This method can be directly combined with traditional lithography techniques and offers a precisely area-selective doping capability, showing great potential in the fabrication of integrated logic circuits.

2.2.3. Buffer layer engineering

Graphene buffer layer. Some metals such as Au and Ag tend to aggregate on the surface of TMDCs to form clusters (Fig. 6a). Such inhomogeneous metal/TMDC interfaces may seriously deteriorate the device performance, which can be improved by inserting a buffer layer between the metal and TMDCs.[92] Graphene is the most widely adopted buffer material owing to its semimetal nature with tunable Fermi level by electrostatic gating.[111,112] The graphene layer can be easily transferred onto the TMDC surface *via* a standard wet/dry transfer method.[113] Compared to intimate metal–MoS$_2$ contact, insertion of a graphene layer between the metal and MoS$_2$ eliminates the metal deposition induced strain and the overheating effect.[92] MoS$_2$ devices with graphene buffer layer have been extensively investigated.[88,112,114–117] Yu *et al.* constructed complementary
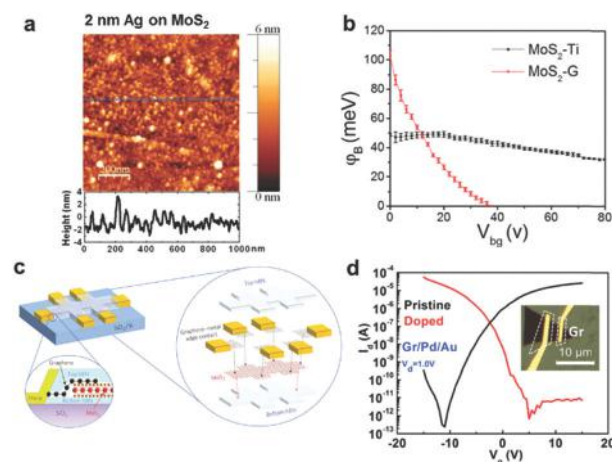

Fig. 6 (a) AFM images of 2 nm Ag on monolayer MoS$_2$. The rms value of roughness is 0.78 nm. (b) The plot of SB height φ_B as a function of V_g for CVD-grown MoS$_2$–graphene and MoS$_2$–Ti junctions. (c) Schematic of a graphene edge-contacted and h-BN-encapsulated MoS$_2$ multi-terminal FET. (d) Transfer characteristics of a graphene-contacted MoS$_2$ before and after AuCl$_3$ doping. Inset shows the optical microscopy image of this device. Reprinted with permission from: (a) ref. 92, Copyright 2013, American Chemical Society; (b) ref. 112, Copyright 2014, American Chemical Society; (c) ref. 114, Copyright 2015, Nature Publishing Group; (d) ref. 88, Copyright 2016, John Wiley and Sons.

logic devices based on chemical vapor deposition (CVD)-grown MoS$_2$/graphene heterostructures and quantitatively analyzed the contact resistance.[112] By fitting the I_d–V_d characteristics in the thermal emission relation of the Schottky junction, the SB height (φ_B) can be extracted, as plotted as a function of back gate voltages (V_g) in Fig. 6b. The φ_B of MoS$_2$/graphene strongly depends on V_g, which dramatically decreases from 110 to 0 meV with V_g increasing from 0 V to 35 V; while the φ_B of MoS$_2$/Ti nearly remains at 40 meV. Such gate-dependent barrier in MoS$_2$/graphene is attributed to the effective tuning of the Fermi level in graphene by V_g with respect to the energy levels of MoS$_2$. Further optimization of the device configuration can be fulfilled by sandwiching the MoS$_2$ channel as well as the graphene electrodes within h-BN layers to reduce the interfacial charge scattering.[114] MoS$_2$/graphene/metal edge-contacts were fabricated *via* side-etching the h-BN/graphene/h-BN stack by O$_2$ plasma (Fig. 6c). The fabricated device shows a high Hall mobility reaching 34 000 cm^2 V^{-1} s^{-1} (6-layer flake) at a temperature below 5 K, leading to the direct observation of Shubnikov–de Haas oscillations on MoS$_2$.[114]

The use of graphene as contact in TMDC devices can lower the contact resistance for both electron and hole transport *via* tuning the Fermi level of graphene by either electrical field[116] or chemical doping.[88] Liu *et al.* used AuCl$_3$ as the electron-acceptor to convert an MoS$_2$ FET from n-type to p-type conduction,[88] but the large SB at the metal/MoS$_2$ contact limits the hole transport in Pd-contacted MoS$_2$ channels. After inserting a graphene buffer layer, the SBs for hole transport are significantly reduced due to the AuCl$_3$-induced downward shift of graphene's Fermi level, hence achieving a high-performance p-type FET (Fig. 6d).[88]

This journal is © The Royal Society of Chemistry 2018

Chem. Soc. Rev., 2018, **47**, 3100–3128 | 3107

Tunnelling buffer layer. In quantum physics, if the width of an energy barrier reaches the quantum limit, wave-like electrons could 'tunnel' the barrier even without sufficient energy to overcome it. This tunnelling effect can be utilized to reduce the contact resistance *via* inserting an ultrathin tunnelling buffer layer between the TMDCs and metal, *i.e.* forming a metal–insulator–semiconductor (MIS) structure. In a MIS structure, the gap between the metal and semiconductor helps to enhance the decay of the electronic wavefunctions, and hence to suppress the metal induced gap states (MIGS) at the metal/semiconductor interface, thereby leading to a largely improved contact. In particular, this method shows advantages in either enhancing the spin polarization[118,119] in the TMDC or improving the contacts in top-gated FETs, where the TMDCs under the metal contact cannot be electrically gated to high doping levels due to the metal contact induced screen effect. Illustrations of the band alignment before and after inserting an insulating buffer layer are shown in Fig. 7a and b, respectively. When the metal electrodes are in direct contact with MoS_2, electrons will fill the surface states and induce strong band bending at the interface, which can be greatly attenuated with the insertion of an insulating buffer layer.[120,121] Meanwhile, the interface dipoles formed across the buffer layer can compensate the applied bias, which further prevents the movement of the Fermi level in MoS_2 towards the charge neutrality point and reduces the SB height.[122] As a result, MIS is an effective structure to obtain MoS_2 FETs with excellent contact performance.

Various insulators, including MgO,[118] TiO_2,[119] Ta_2O_5[123] and h-BN[124,125] have been adopted as tunnelling buffer layers to modify the contacts in MoS_2 devices. Chen *et al.* reported that the insertion of a 2 nm MgO thin film between MoS_2 and Co can greatly reduce the SB height from 60.6 to 9.7 meV.[118] Similarly, the introduction of a TiO_2 thin layer shows a dramatic decrease of the contact resistance by two orders of magnitude, as exhibited in Fig. 7c and d[119]. Although metal oxides form effective tunnelling barriers between metals and TMDCs, the lack of surface dangling bonds on TMDCs induces the inhomogeneous growth of the oxide layer,[126,127] and interfacial charge transfer may occur between the metal oxide and TMDCs, deteriorating the intrinsic transport properties of the TMDCs.[107,128,129] As an alternative with an atomically-smooth and inert surface, a h-BN buffer layer has been used as a tunnelling buffer layer in MoS_2 to improve the electrical contact.[124,125] As illustrated in Fig. 7e and f, the initial SB height of $\sim$158 meV (MoS_2/Ni) can be greatly reduced to 31 (38) meV by adding 1–2 (3–4) layers of h-BN. Given that tunnelling resistance is mainly determined by the h-BN thickness, the device with a monolayer h-BN buffer layer possesses the best device performance, which largely reduces the contact resistance from 5.1 kΩ μm to 1.8 kΩ μm.[124] With the development of CVD growth of large scale monolayer h-BN[130] and mature transfer technologies, the h-BN/TMDC heterostructure shows great potential in future 2D material-based electronics.

Other buffer layers. Very recently, substitutionally-doped TMDCs have been synthesized by chemical vapor transport (CVT) to serve as the buffer layer to improve the contact performance of TMDC devices.[131] By applying p-doped $Nb_{0.005}W_{0.995}Se_2$ as a contact, the WSe_2 FET device exhibits a contact resistance as low as $\sim$0.3 kΩ μm, a high on/off ratio larger than 10^9, and high drive currents exceeding 320 μA μm^{-1}. Furthermore, this strategy is able to obtain high-performance hole transport in MoS_2 FETs *via* inserting a p-doped buffer layer $Nb_{0.005}Mo_{0.995}S_2$, showing a high hole field-effect mobility of $\sim$180 and 2800 cm^2 V^{-1} s^{-1} at room temperature and 5 K, respectively. Using the plasma-enhanced ALD-CVD technique, an interfacial transition regime of $W_xNb_{1-x}Se_2$ can be introduced between semiconducting WSe_2 and metallic $NbSe_2$.[132] The SB heights in Pd/WSe_2, $Pd/NbSe_2/WSe_2$ and $Pd/NbS_2/W_xNb_{1-x}Se_2/WSe$ are 326, 199 and 176 meV, respectively. Lowering the SB and tunnelling at the metal/$W_xNb_{1-x}Se_2$/TMDCs are considered to be the two main reasons for the improvement in the contact performance in these transition-regime-contained van der Waals heterostructures.

2.3. Dielectric/TMDC interface engineering

In early studies, the field-effect electron mobility for monolayer MoS_2 was found to be less than 10 cm^2 V^{-1} s^{-1} at room temperature in commonly used back-gated FET configurations on an SiO_2 dielectric,[133] far less than the theoretical predictions.[33,134] This is mainly attributed to the serious extrinsic scattering of charge carriers during the transport, including the scattering induced by charge impurities (Coulomb impurities, CIs), trapping states at the interface, defects of TMDCs and remote
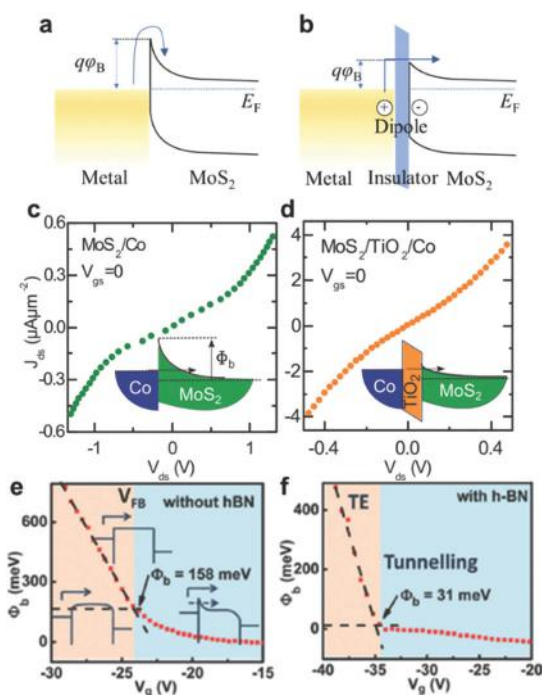

Fig. 7 Band alignment of a metal/MoS_2 contact (a) before and (b) after inserting an insulating layer. Transfer characteristics of the MoS_2 devices with (c) Co and (d) TiO_2/Co contact. The plot of SB heights at different gate voltages for the MoS_2 device (e) without and (f) with a h-BN buffer layer, respectively. Reprinted with permission from: (c and d) ref. 119, Copyright 2014, American Chemical Society; (e and f) ref. 124, Copyright 2016, John Wiley and Sons.

3108 | *Chem. Soc. Rev.*, 2018, **47**, 3100–3128

This journal is © The Royal Society of Chemistry 2018

surface optical (SO) phonons.[32,114,135–138] CIs originate from a variety of impurity sources, such as the residual metal ions in the dielectric, impurities at the 2D material/substrate interface and residual solvent or adsorbed gas molecules during the device fabrication, which are deemed to be point charges and interact with e^-/h^+ in the 2D material through long range Coulomb interactions. Defects refer to the imperfection or disorder of the crystal lattice, such as atomic vacancies/ interstitials and grain boundaries, which will be discussed in Section 3. SO phonons come from the polar vibrational modes in the dielectric, which can be excited by electrons in the conduction channel and in turn degrade the mobility in the channel. All the aforementioned scattering processes can be suppressed by lowering the temperature.

A comprehensive experimental and theoretical study of electron transport in defect-rehabilitated monolayer MoS_2[136] by Yu et al[139] indicates that the mobility of MoS_2 is dominated by CI scattering if the CI concentration is more than 0.3×10^{12} cm^{-2}, whereas the use of a high-k dielectric like HfO_2 can effectively screen the CI scattering. Otherwise, the SO phonon scattering dominates the charge transport with the CI concentration below 0.3×10^{12} cm^{-2} and a low-k dielectric like SiO_2 is preferred, as shown in Fig. 8a. From the theoretical simulation, the electron mobility of MoS_2 is limited by ionized impurity scattering at low temperature; while the combined homopolar and the polar-optical phonon scattering dominate at room temperature.[143]

2.3.1. High-k dielectric. It has been predicted that deposition of a high-k dielectric like HfO_2 is an effective method to enhance the carrier mobility in 2D semiconductors,[144] as

further demonstrated by several experimental studies.[13,136,143,145–147] Wang's group has performed a series of detailed investigations in this field.[139,145,146] They first developed a defect-healing method by thiol chemistry to get rid of the defect scattering from S vacancies, which will be discussed in Section 3.3.1.[136] Under the same carrier density $n = 7.0 \times 10^{12}$ cm^{-2}, the charge carrier field-effect mobility of monolayer WS_2 on Al_2O_3 ($\varepsilon = 10$) reaches 49 cm^2 V^{-1} s^{-1} at room temperature, twice the value on SiO_2 ($\varepsilon = 3.9$),[146] which can be further improved to 83 cm^2 V^{-1} s^{-1} by thiol functionalization. Furthermore, the room temperature field-effect mobilities of monolayer MoS_2 on HfO_2 ($\varepsilon = 16.5$), Al_2O_3 and SiO_2 at the same carrier concentration are compared and presented in Fig. 8b, which clearly shows that mobility increases with the dielectric constant.[139] This significant mobility enhancement by high-k dielectrics can be attributed to the reduction of CI scattering and the charge traps, as well as possible modification of the phononic dispersion relation.[13,139,145,146] Temperature-dependent transport measurements on dual-gated MoS_2 (SiO_2 and HfO_2 as bottom and top gate, respectively) further confirm the effective depression of CI scattering by using a high-k dielectric, as revealed by the monotonic increase of Hall mobility with decreasing temperature in Fig. 8d, in sharp contrast to the temperature dependence of a bottom-gated device in Fig. 8c.[140,148] More interestingly, the charge carrier density of monolayer MoS_2 can be tuned to a high doping level up to $\sim 3.6 \times 10^{13}$ cm^{-2} in dual-gated FETs, thus inducing the transition from an insulating to a metallic state due to the strong electron–electron interaction.[149] The success of the effective control of device performance via high-k dielectrics
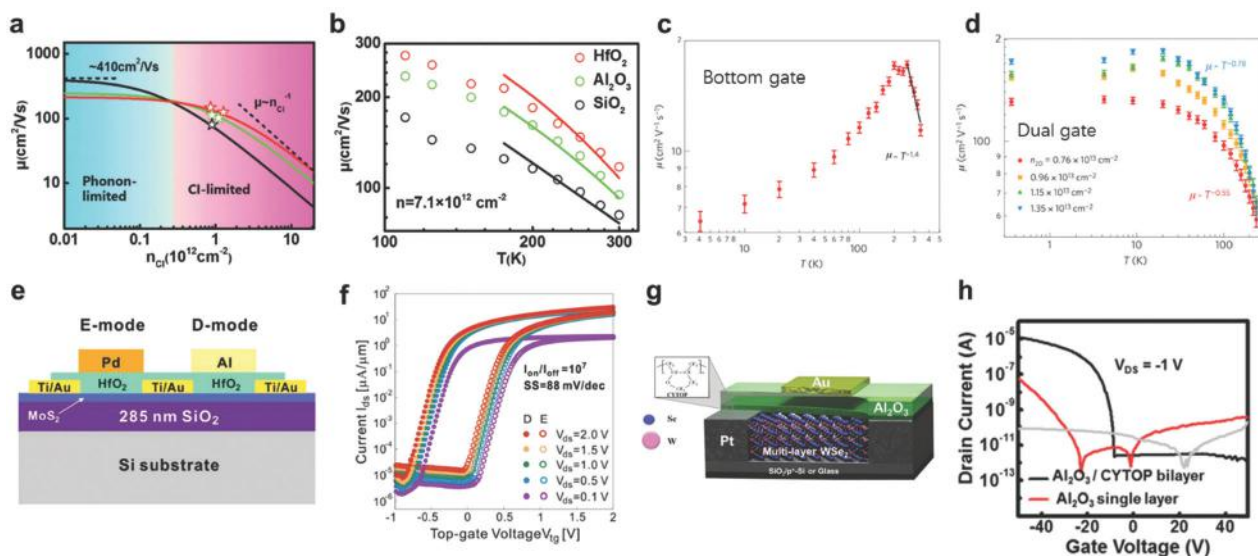

Fig. 8 (a) The simulated charge carrier mobility as a function of CI concentration for TMDC devices on SiO_2 (black), Al_2O_3 (green), and HfO_2 (red). (b) Field-effect mobility as a function of temperature for three devices on SiO_2 (black), Al_2O_3 (green), and HfO_2 (red), respectively. Solid lines are the modelling results. Temperature dependent field-effect mobility of monolayer MoS_2 in (c) bottom- and (d) dual-gated MoS_2 FETs, respectively. (e) Schematic illustration of a HfO_2-covered MoS_2 FET with Pd (E-mode) and Al (D-mode) top electrodes. (f) The transfer characteristics of D-mode and E-mode bilayer MoS_2 FETs. (g) Schematic drawing of a top-gated FET with a bilayer CYTOP/Al_2O_3 top gate dielectric. (h) Transfer characteristics of a 4L WSe_2 FET after Al_2O_3 deposition with and without a CYTOP buffer layer. Reprinted with permission from: (a and b) ref. 139, Copyright 2016, John Wiley and Sons; (c and d) ref. 140, Copyright 2013, Nature Publishing Group; (e and f) ref. 141, Copyright 2012, American Chemical Society; (g and h) ref. 142, Copyright 2015, John Wiley and Sons.

This journal is © The Royal Society of Chemistry 2018

Chem. Soc. Rev., 2018, 47, 3100–3128 | 3109

provides the opportunity to incorporate this dielectric engineering into integrated logic circuits.[141,150,151] As shown in Fig. 8e and f, transistors with both negative (D-mode) and positive (E-mode) threshold voltages are achieved on a single bilayer MoS_2 using Al and Pd gate electrodes on 20 nm HfO_2, respectively.[141] The origin of the threshold voltage difference between D- and E-mode transistors can be understood by a band alignment process in an MIS structure (Fig. 7a and b). Based on the prototype device, multiple transistors can be integrated to achieve various functional devices, including inverters, NAND gates, static random-access memory and five-stage ring oscillators.[141]

Although high-quality metal oxide dielectrics can be grown by ALD, several studies report the inhomogeneity of grown dielectrics owing to the lack of dangling bonds on TMDC surfaces, which may lead to leakage from the gate electrode.[96,127] A possible solution is to chemically pre-treat the surface of TMDCs[152–154] or insert a buffer layer before the growth of the high-k dielectric.[96,142] Zou et al. built up MoS_2 FETs by adding an ultrathin metal oxide (MgO, Al_2O_3, Y_2O_3) buffer layer between MoS_2 and HfO_2, which shows a good device performance with a high on/off ratio larger than 10^8 as well as a near-ideal subthreshold swing of ~65 mV dec^{-1}.[126] This method is also applicable to other TMDCs like HfS_2.[148] In addition, during the traditional ALD process, the precursor reacts with water at high temperature, e.g. 250–300 °C for Al_2O_3, which may generate hydrogen atoms that diffuse into the TMDCs and lead to n-type doping.[142] The use of an organic fluoropolymer (CYTOP) as a buffer layer in WSe_2 devices can eliminate the n-type doping effect during the ALD growth of Al_2O_3, thus retaining its unipolar hole transport properties, as shown in Fig. 8g and h.

Moreover, as CYTOP is a low-k dielectric, it will not induce serious SO phonon scattering as found in devices with high-k dielectrics.[138,142] Other surface treatments, like ultraviolet-O_3 exposure to form oxygen–S bonds at the MoS_2 surface[153] or oxygen plasma pre-treatment to provide dangling bonds can also facilitate the growth of high-k dielectrics on TMDCs.[152,154]

2.3.2. Other solid dielectrics. Another dielectric engineering strategy is using a better bottom gate dielectric to replace the conventional solid-state dielectric SiO_2 that limits the device performance of TMDCs due to the existence of severe dangling bonds, impurities and surface states. For example, the carrier mobility of TMDCs is limited by the scattering from the charged surface states and impurities,[155] surface roughness, and surface optical phonons of SiO_2, while the photoresponsivity and photoresponse time of TMDCs can also be affected due to the carrier scattering and trap states on the SiO_2 substrate. The slow photoresponse in MoS_2 photodetectors may result from charge trap states at the MoS_2/SiO_2 interface with surface-bound water.[156] h-BN, as a layered insulator with a bandgap of ~6 eV, features an atomic flat surface without dangling bonds. Therefore, it has been widely used as a dielectric material in graphene electronics[157] and can be an appropriate choice for TMDCs. MoS_2 devices with different back gating architectures of MoS_2/SiO_2 (denoted as MS), MoS_2/h-BN/SiO_2 (MB) and $MoS_2/$h-BN/graphene (MBG)[19] have been systematically investigated. The h-BN-supported devices (MB and MBG) possess a much higher carrier mobility and smaller hysteresis than the MS device (Fig. 9a), owing to the atomically flat surface and low-density of charge trapping sites in h-BN. In addition, high photoresponsivity and short photoresponse time of TMDCs can be obtained by using h-BN as the substrate due to reduced scattering from the
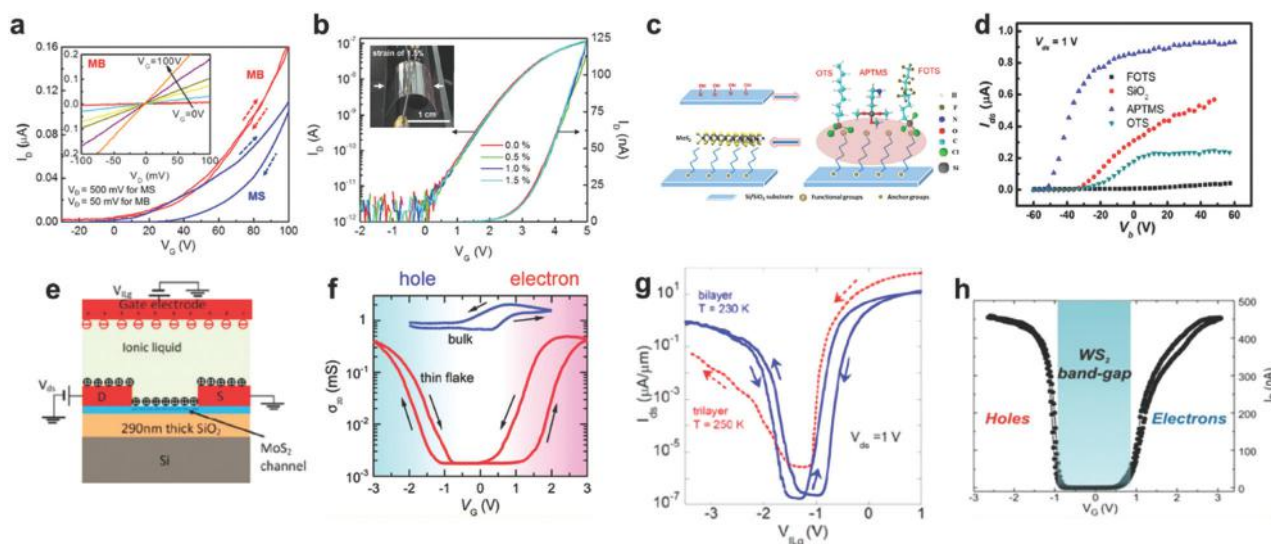

Fig. 9 (a) Transfer characteristics of MoS_2 FETs with different back gating structures of MoS_2/SiO_2 (MS) and MoS_2/h-BN/SiO_2 (MB). (b) Transfer characteristics of the flexible MoS_2/h-BN/graphene (MBG) device with respect to the bending strain. (c) Schematic illustration of the SiO_2 dielectric modified by self-assembled monolayers (SAMs). (d) Transfer characteristics of few-layer MoS_2 FETs on SAM-modified SiO_2 substrates. (e) Schematic illustration of the working principle of an ionic-liquid-gated MoS_2 FET. Transfer characteristics of ionic-liquid-gated (f) few-layer, (g) bilayer and trilayer MoS_2 FETs, and (h) a few-layer WS_2 FET. Reprinted with permission from: (a and b) ref. 19, Copyright 2013, American Chemical Society; (c and d) ref. 73, Copyright 2013, American Chemical Society; (e and g) ref. 109, Copyright 2013, American Chemical Society; (f) ref. 167, Copyright 2012, American Chemical Society; (h) ref. 172, Copyright 2012, American Chemical Society.

impurities and trap states in the substrate.[60,158,159] The MBG structure can be easily integrated into flexible electronic devices by transferring it onto a flexible polyethylene naphthalate (PEN) substrate, where the bending of the device (up to 1.5% strain) would not disturb the output signal (Fig. 9b).[19] Double-face encapsulation by h-BN would further increase the device performance and side contact is needed[114,160] (Fig. 6c). Other solid dielectrics like PMMA[161] and parylene-C,[162] have also been utilized in TMDC devices to enhance their performance. On the other hand, the use of dielectric materials functionalized by SAMs can effectively dope the TMDCs from the substrate by choosing suitable terminal groups with different dipole moments.[73] For example, fluoroalkyltrichlorosilane-SAM and 3-(trimethoxysilyl)-1-propanamine-SAM on the substrate could serve as dopants to either p- or n-dope MoS_2, respectively (Fig. 9c and d). SAMs not only effectively dope the upper TMDCs in a controlled manner, but also form an ultrasmooth surface to reduce the interfacial impurity scattering, thus enhancing the transport performance of TMDC-based devices.

Owing to the weak dielectric screening and strong quantum confinement in the 2D limit, the exciton binding energies in TMDCs ($\sim$370 meV for monolayer WSe_2) are over an order of magnitude larger than those in the conventional inorganic semiconductors, which are also highly sensitive to the local dielectric environment.[163–165] Even though excitons are confined in TMDC monolayers, the electric field of excitons can permeate into the local surroundings and can be effectively screened by top or bottom attached few-layer graphene and h-BN, leading to a decrease in both the bandgap and exciton binding energy by several hundreds of meV.[166]

2.3.3. Ionic liquid gating. As a liquid-phase dielectric, ionic liquids feature an electric double layer (EDL) structure, which provides a huge capacitance to accumulate the charge carriers that is far beyond those of conventional solid dielectrics.[167] A schematic device structure with ionic liquid gating is shown in Fig. 9e. With this ultra-high electron-drawing ability, ionic liquids have been used to induce insulator-to-metal transitions in ZnO[168] as well as superconductivity in $SrTiO_3$.[169] Zhang et al. used DEME-TFSI (N,N-diethyl-N-methyl-N-(2-methoxyethyl) ammonium bis (trifluoromethyl-sulfonyl) imide) as an ionic liquid dielectric[167] in MoS_2 FETs. The device exhibits ambipolar transport characteristics with a field-effect hole and electron mobility of $\sim$86 and 44 cm^2 V^{-1} s^{-1}, respectively, while both the hole and electron carrier concentration could reach as high as $\sim$10^{14} cm^{-2}, which is 1 order of magnitude higher than in the MoS_2 device with an SiO_2 dielectric.[170] However, this ion-gel-gated device suffers from a low on/off ratio of $\sim$10^2. The ultrathin EDL can reduce the width of the SB by strong band bending near the contacts, thus facilitating the tunnelling of both holes and electrons through the metal/semiconductor interface. Hence, the injection of both carriers occurs via thermal-assisted tunnelling rather than by a thermionic emission process.[171] Perera et al. also used DEME-TFSI ionic liquid as the dielectric in bi- and tri-layer MoS_2 FETs,[109] achieving a high on/off ratio > 10^7 (10^4) for electrons (holes), a subthreshold swing of about 50 mV dec^{-1} at 250 K, and a field-effect

mobility of up to 220 cm^2 V^{-1} S^{-1} at 77 K[108] (Fig. 9g). The device performance of an ion-liquid-gated device can be further enhanced by replacing the metal contacts with graphene, by taking advantage of the gate-tunable Fermi level, as previously discussed in Fig. 6b. Chuang et al. fabricated WSe_2 FETs with h-BN-passivated channels and ionic liquid-gated graphene contacts, showing high hole and electron field-effect mobilities of 270 and 330 cm^2 V^{-1} s^{-1} at 77 K, respectively.[116] Moreover, the ionic-liquid-gated WS_2 device shows stable and hysteresis-free ambipolar characteristics with steep subthreshold slopes for both electrons and holes (Fig. 9h), owing to the perfect electrostatic coupling between the ionic liquid gate and the semiconductor channel.[172] This feature permits the quantitative determination of the WS_2 bandgap using the equation:

$$\Delta V_{gap} = V_{TH}^e - V_{TH}^h,$$

where V_{TH}^e and V_{TH}^h are threshold voltage for the electron and hole side, respectively. The bandgap is calculated to be $\sim$1.4 eV, consistent with the previously reported values (1.3–1.35 eV).[12,173]

Owing to the super-high carrier concentration achieved by ionic liquid gating, many interesting phenomena such as rectifying behavior,[174] metal–insulator transition,[116] phase transition,[175,176] charge-density wave[177] and superconductivity[178,179] have been observed in ionic liquid gated-TMDCs. As a result, ionic liquid gating has emerged as an essential tool to investigate 2D material-based many-body effects under extreme conditions.

2.3.4. Ferroelectric dielectrics. Ferroelectric materials are a family of materials with intrinsic ferroelectricity. Analogous to ferromagnetic materials that feature a permanent magnetic momentum, ferroelectric materials have a spontaneous electric polarization even at zero bias, which can be divided into polarization up (P_{up}) and down (P_{down}) states as shown in Fig. 10a. This polarization can be reversed by an external electrical field, leading to great potential applications in memory devices. Note that ferroelectric materials are high-k insulators, which makes them a potential dielectric material for constructing 2D material-based devices with different functionalities, such as low power transistors, memory devices, photodetectors etc.

FET devices with low power dissipation are desirable for future electronic devices, which can be realized by lowering the operation voltage.[180–182] The operation voltage strongly depends on the subthreshold swing of FETs, which cannot be lower than 60 meV dec^{-1} at room temperature under thermodynamic equilibrium. A possible way to overcome this limitation is to replace the traditional insulating dielectric with a ferroelectric material that acts as a negative capacitor.[183] A typical device structure is shown in Fig. 10b, where the ferroelectric material $Hf_{0.5}Zr_{0.5}O_2$ (HZO)[184,185] and Al_2O_3 are used as dielectric and capacitance matching materials, respectively. The use of HZO in MoS_2 FETs leads to a high working current of 510 μA μm^{-1} with an outstanding subthreshold swing of 57.6 and 52.3 mV dec^{-1} for forward and reverse

This journal is © The Royal Society of Chemistry 2018

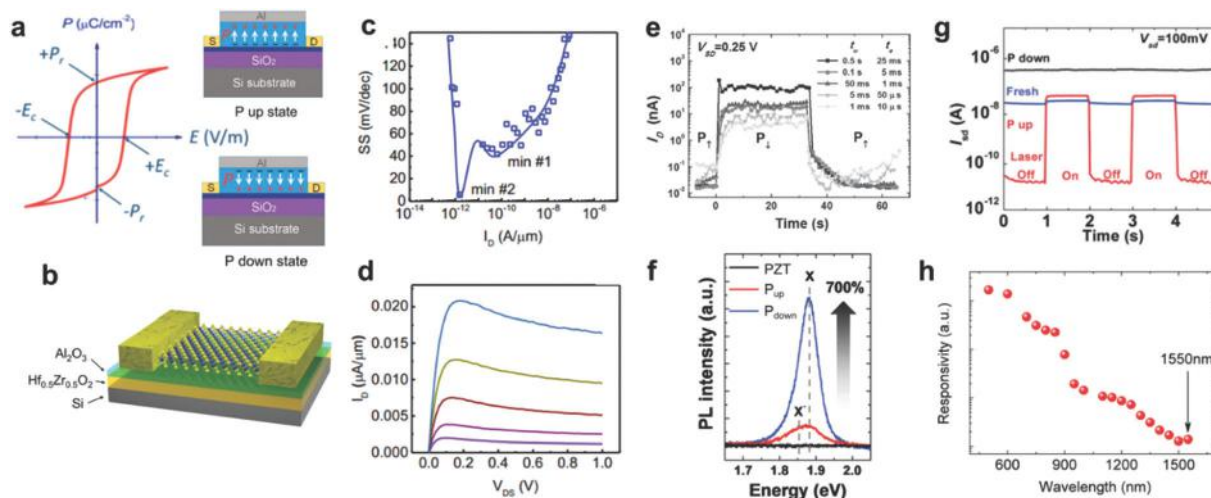*Chem. Soc. Rev.*, 2018, **47**, 3100–3128 | **3111**

Fig. 10 (a) Left: Typical ferroelectric hysteresis curve. P_r and E_c are the remnant polarization and coercive electric field, respectively. Right: A schematic of the FET devices with a ferroelectric dielectric of polarization up and down, respectively. (b) Schematic illustration of a MoS_2 FET with an HZO ferroelectric film and Al_2O_3 dielectric. (c) The plot of subthreshold voltage with respect to the drain current I_d and (d) $I-V$ characteristics at V_g from -0.65 V to -0.55 V in the device shown in (b). (e) Time-dependent relaxation curves in a WSe_2 FET with a PZT dielectric obtained after pulsed gating at on (P_{down}) states and following off (P_{up}) states. (f) PL spectra measured from the MoS_2 monolayer with a PZT dielectric at both polarization states. In a MoS_2 FET with a P(VDF-TrFE) dielectric, (g) photoswitching behaviors at three states, fresh, P_{down} and P_{up}, respectively, and (h) photoresponsivity as a function of incident light wavelength from 500 to 1550 nm under the P_{up} state. Reprinted with permission from (a, g and h) ref. 194, Copyright 2015, John Wiley and Sons; (b–d) ref. 186, Copyright 2018, Nature Publishing Group; (e and f) ref. 191, Copyright 2016, John Wiley and Sons.

sweeps, respectively.[186] This can be further reduced to as low as 5.6 mV dec^{-1} (min #2 in Fig. 10c) and is much smaller than 80–90 mV dec^{-1} realized in Al_2O_3 back-gated devices. The significant reduction of subthreshold swing results from the switching between two polarization states of HZO. Meanwhile, a negative differential resistance[186] is observed in this device (Fig. 10d), showing great potential in high-frequency electronics, *i.e.* Gunn diodes.

TMDC-based memory devices can be constructed by utilizing ferroelectric materials with gate-tunable polarization effects as dielectrics.[187–191] For instance, Ko *et al.* used MoS_2 or WSe_2 in combination with $Pb[Zr_{0.2}Ti_{0.8}]O_3$ (PZT) to fabricate non-volatile memory devices, presenting a low switching voltage (<2.5 V), high on–off ratio ($>10^4$), superior data retention (>10 d) and fast on/off switching (<25 ms), as shown in Fig. 10e, which are comparable to conventional ferroelectric materials.[191] More interestingly, there exists a non-volatile modulation of PL intensity (increased by over 7 times) in monolayer MoS_2 when switching the polarization from the P_{up} to P_{down} state, in agreement with the transition from negative trion recombination to exciton recombination.[55,58,69] In addition, the photodetecting performance of MoS_2 with ferroelectric films (P(VDF-TrFE))[192,193] as dielectrics was investigated by Wang *et al.*[194] In the P_{up} state, the electrons in MoS_2 are largely exhausted, leading to an ultra-high signal-to-noise ratio of $\sim 10^3$; while the fresh and P_{down} state devices give a negligible photocurrent (Fig. 10g). Moreover, the strong electrical field induced by the P_{up} ferroelectric film decreases the bandgap of MoS_2, making the (P(VDF-TrFE))/MoS_2 photo-transistor operate in a broad spectrum range up to 1.55 μm (Fig. 10h).[194]

3. Defect engineering of TMDCs and its application in electronic and optoelectronic devices

3.1. Structural defects in TMDCs

The structures of TMDCs always contain abundant and different types of defects, such as vacancies, adatoms, edges, grain boundaries, and substitutional impurities, which play significant roles in electronics and optoelectronics. Below, we will introduce several types of structural defects that are frequently adopted for defect engineering.

3.1.1. Point defects. Vacancies, including chalcogen and transition metal vacancies and their related coalescence and reconstruction (Fig. 1d), are the most commonly investigated defects in TMDCs.[27,195,196] High resolution transmission electron microscopy (TEM) characterization reveals that there is a high density ($\sim 10^{13}$ cm^{-2}) of S vacancies in single layer mechanically exfoliated MoS_2 (Fig. 11a).[32] According to theoretical calculations, these S vacancies can induce localized states in the bandgap of MoS_2 as shown in Fig. 11b. S vacancies as short-range disorders and electron donors are one of the key extrinsic factors leading to low mobility and n-type doping of MoS_2.[30,32,197] On the other hand, scanning tunnelling microscopy (STM) and spectroscopy (STS) characterization reveals that the localized states appear around the transition metal (tungsten, W) vacancies in a WSe_2 monolayer as shown in Fig. 11c and d, and lead to p-type doping.[197] Since excitons can be localized by defect states, emission from bound excitons is detected in TMDCs, especially at low temperature.[198] Fig. 11e gives electronic (upper) and excitonic (lower) schematic diagrams of the WSe_2 monolayer, respectively.[197] Polarization-resolved PL spectra of a WSe_2
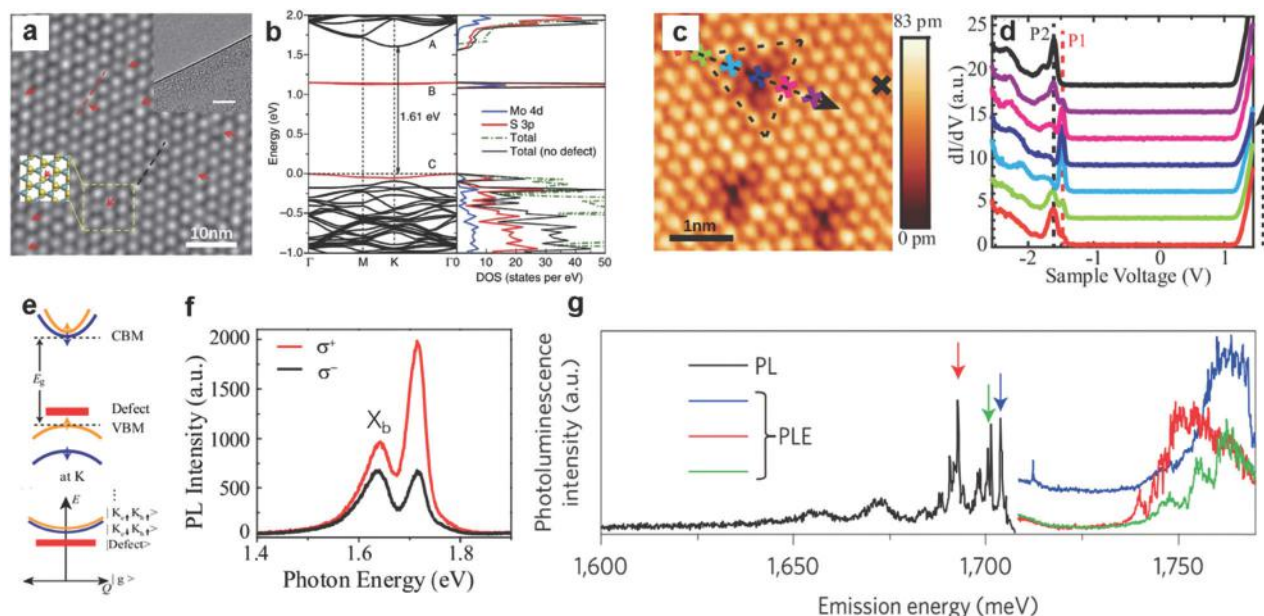
Fig. 11 (a) TEM characterization of S vacancies in a MoS_2 monolayer. (b) Band structure and partial density of states of the MoS_2 monolayer (5×5 supercell with an S vacancy). The localized states are highlighted by red lines. (c) Atomically resolved STM imaging of the WSe_2 monolayer with W vacancy at bias voltage of -1.2 V. (d) STM spectra of positions marked with crosses in (c). (e) Electronic (upper) and excitonic (lower) schematic diagrams of the WSe_2 monolayer with W vacancies. (f) Polarization-resolved PL spectra of the WSe_2 monolayer under σ^+ detection. The red and black lines correspond to σ^+ and σ^- circularly polarized light excitation. (g) The PL spectrum of WSe_2 with isolated defects and PLE of the sharp emission lines. Reprinted with permission from: (a and b) ref. 32, Copyright 2013, Nature Publishing Group; (c–f) ref. 197, Copyright 2017, American Physical Society; (g) ref. 200, Copyright 2015, Nature Publishing Group.

monolayer containing W vacancies are shown in Fig. 11f. Due to the high density of defects in the CVD sample, a broadened defect activated PL peak (X_b) appears.[197] The band-edge of monolayer TMDCs is located at energy degenerate valleys ($\pm K$) at the corners of the hexagonal Brillouin zone. The absorption of left and right-handed light ($\sigma\pm$) is different for monolayer TMDCs and the confinement of electrons and holes to the $\pm K$ valleys gives rise to valley excitons and trions. The circular polarization (P) of free excitons (49% at $\sim$1.72 eV) is much larger than that of bound excitons (16% at $\sim$1.64 eV) and valley coherence of the bound excitons is absent. This indicates that the trigonal symmetry of the single W vacancy defect is reduced.[197] When suitably isolated, defects can also act as single quantum emitters (SQEs).[199–201] Sharp emission lines appear in the PL spectrum of WSe_2 at low temperature and PL excitation (PLE) spectra of these lines show absorption resonances in accordance with the absorption band of WSe_2, as shown in Fig. 11g.[200] Furthermore, compressive strain can also be generated by introducing S vacancies into a MoS_2 monolayer after electron beam exposure[202] and local bandgap modification is achieved, which is confirmed by the blue shift of the PL peak in the exposed areas.[203]

Substitutional impurities (Fig. 1d), for example, isoelectronic substitutions, are another typical form of defects in TMDC materials.[31] The transition metal or chalcogenide or both of them in TMDCs can be substituted by an isoelectronic atom during CVD growth and different types of alloys are prepared. Composition-dependent bandgap emission can be observed by employing isoelectronic substitution, ranging from $\sim$1.6

to $\sim$2 eV for sulphides (MoS_2, WS_2) and selenides ($MoSe_2$, WSe_2). A scanning transmission electron microscopy (STEM) image of transition metal isoelectronic substitution ($Mo_{1-x}W_xS_2$ monolayer) after fast Fourier transform (FFT) filtering is shown in Fig. 12a, which exhibits two types of atoms with different contrasts.[204] W and Mo atoms are confirmed by electron energy loss spectroscopy (EELS) characterization as shown in Fig. 12b.[204] Fig. 12c gives the STEM image of chalcogenide isoelectronic substitution ($WS_{2x}Se_{2-x}$ monolayer).[36] The S, Se and W element distribution is characterized by Energy-dispersive X-ray spectroscopy (EDS) elemental mapping (Fig. 12d), revealing composition uniformity.[36] In addition to substitution with randomly distributed elements, a Janus monolayer (such as SMoSe or SeMoS) of TMDCs breaking the out-of-plane structural symmetry can be prepared by replacing the top-layer S (Se) with Se (S) in monolayer MoS_2 ($MoSe_2$).[205,206] The fabrication process of SeMoS is as follows: hydrogen plasma is employed to strip off the top-layer S atoms of MoS_2 and replace the S atoms with hydrogen (H) atoms, forming a Janus HMoS monolayer; thermal selenization then allows Se atoms to replace the H atoms, forming a Janus SeMoS monolayer (Fig. 12e).[205] The PL spectra (Fig. 12f) of MoS_2, HMoS, and SeMoS agree well with the theoretical calculations, indicating the metallic properties of HMoS, recovering from HMoS to MoS_2 after sulfurization, and the formation of the Janus SeMoS monolayer.[205] The study of Janus structures provides a novel material with symmetry breaking in the out-of-plane direction and shows promising applications in light–matter interactions, nanoelectromechanical devices, catalysis and spintronics.[205,206] For example, the catalytic
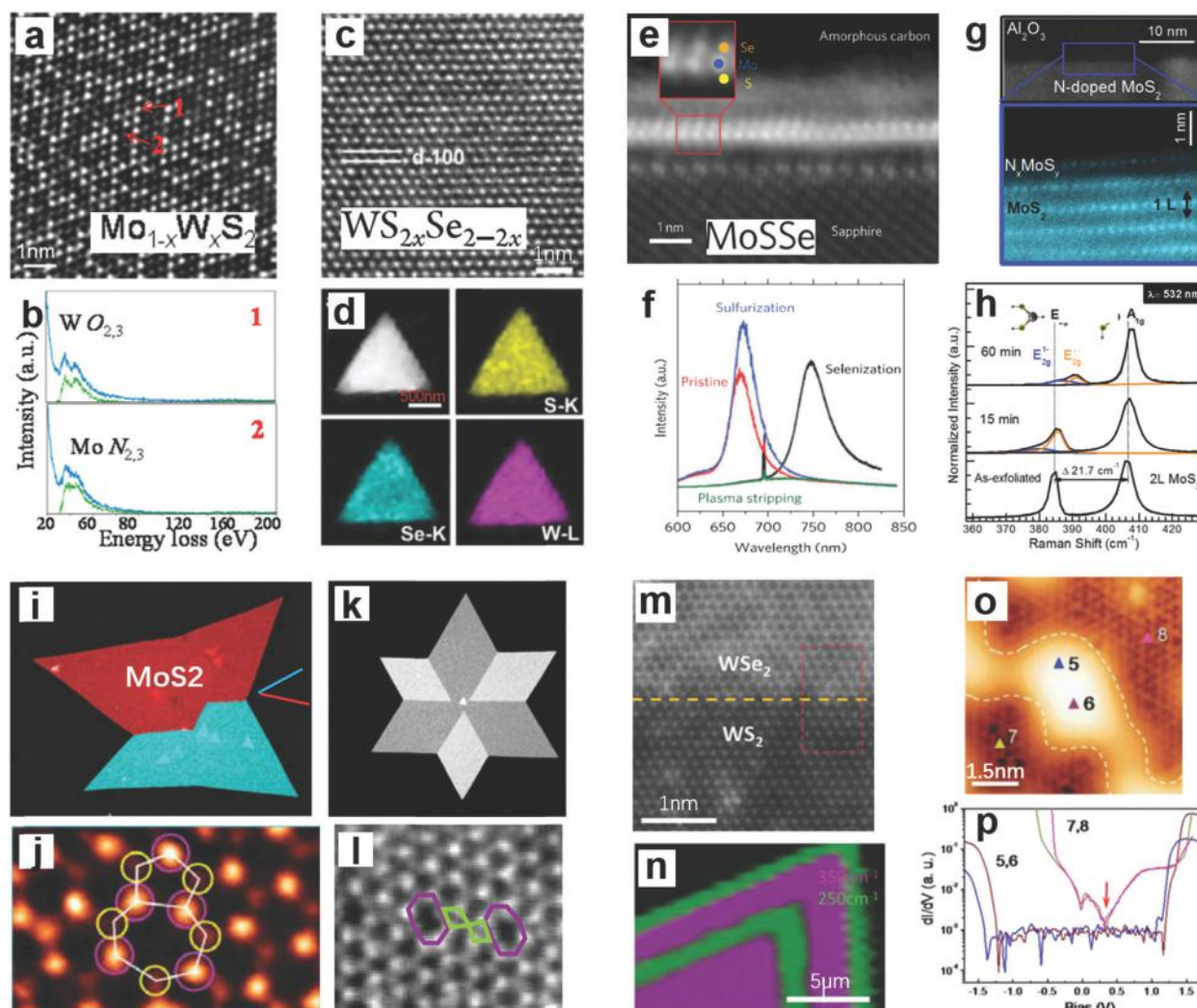
This journal is © The Royal Society of Chemistry 2018

Chem. Soc. Rev., 2018, 47, 3100–3128 | 3113

Fig. 12 (a) TEM image of a $Mo_{1-x}W_xS_2$ monolayer. (b) EELS characteristics of W and Mo atoms indicated as ''1'' and ''2'' in (a), respectively. (c) TEM image of a $WS_{2x}Se_{2-2x}$ nanosheet. (d) High-angle annular dark-field image and EDS mapping of a $WS_{2x}Se_{2-2x}$ domain. (e) TEM image of a Janus monolayer (MoSSe). (f) PL spectra of pristine MoS_2 and those after H_2 plasma treatment, sulphurization and selenization, respectively. (g) TEM images of N-doped MoS_2. (h) Raman spectra of the as-exfoliated MoS_2 flakes and after sequential N_2 plasma exposures of 15 and 60 min, respectively. (i and k) TEM images of polycrystalline MoS_2 with a tilt (i) and mirror (k) twin boundary. (j and l) 8–4 (j) and 7–5 (l) membered rings in the grain boundary. (m) High resolution TEM image of a WS_2–WSe_2 lateral heterostructure. (n) Raman image at 250 and 350 cm^{-1} of a WS_2–WSe_2 superlattice structure. (o) STM image of monolayer MoS_2 after local phase-transition treatment. (p) dI/dV spectra recorded at different locations (triangles marked as 5, 6, 7, 8) in (o). Reprinted with permission from: (a and b) ref. 204, Copyright 2013, American Chemical Society; (c and d) ref. 36, Copyright 2016, American Chemical Society; (e and f) ref. 205, Copyright 2017, Nature Publishing Group; (g and h) ref. 207, Copyright 2016, American Chemical Society; (i–l) ref. 29, Copyright 2013, Nature Publishing Group; (m and n) ref. 208, Copyright 2017, American Association for the Advancement of Science; (o and p) ref. 209, Copyright 2017, American Chemical Society.

activity of Janus structures for the hydrogen evolution reaction (HER) is superior and the high activity may originate from the synergistic effects of the intrinsic defects and structural strain.[206] Another kind of substitutional impurity is substitutional dopants with non-isoelectronic elements, such as nitrogen (N), phosphorus (P) and niobium (Nb). These dopants are very efficient to tune the carrier concentration, mobility and interface properties of TMDCs. The cross-section STEM images of N-doped MoS_2 in Fig. 12g reveal the substitution of S atoms by N atoms after N_2 plasma irradiation.[207] Raman spectra of MoS_2 before and after such treatment are shown in Fig. 12h. The E_{2g}^1 peak splitting is attributed to the presence of strain and

a shift of the out-of-plane vibrational mode A_{1g} illustrates charge doping effects for the N-doped MoS_2 system.

3.1.2. Line defects. Line defects (one-dimensional defects) are also an important type of defect that can strongly influence the properties of CVD-grown TMDCs, including grain boundaries and lateral heterojunctions.[29,208,210] Fig. 12i and k show dark-field TEM images of a polycrystalline MoS_2 sample grown by CVD, with a tilt (Fig. 12i) and mirror (Fig. 12k) twin boundary, respectively.[29] Tilt and mirror twin boundaries are stitched together by lines of 8- and 4- (Fig. 12j) or 7- and 5-membered rings (Fig. 12l). The mirror boundary can induce quenching of the PL intensity, while the tilt boundary shows a strong enhancement in

3114 | Chem. Soc. Rev., 2018, 47, 3100–3128

This journal is © The Royal Society of Chemistry 2018

emission strength. The defects in the mirror or tilt boundaries are Mo or S rich, which can n- or p-dope the boundary, respectively.[29] Since MoS_2 is commonly n-doped, the depletion of electrons by p-doping in the tilt boundary would cause a transformation from trion to neutral exciton emissions, and hence the enhancement of PL efficiency. In addition, strain around the boundaries can also modulate the PL emission.[29]

Furthermore, if two TMDCs with the same crystal orientation are combined together, a lateral heterojunction can be realized. Though p–n junctions can also be formed by a vertical heterostructure, there are problems including unwanted trapping states, lattice mismatch, and spatial inhomogeneity.[211] In-plane p–n junctions formed by lateral heterostructure can possibly overcome these challenges. The atomic structure of the WS_2–WSe_2 lateral heterostructures has been characterized by STEM (Fig. 12m), indicating a seamless connection and an atomically sharp 'interline' or interface,[197] which is critical for fabricating high-performance lateral heterostructures. The PL and Raman mapping (Fig. 12n) further confirm the formation of WS_2–WSe_2 lateral heterostructures and the sharp transition from WS_2 to WSe_2 at the interface.[208]

3.1.3. Local phase transition. Under certain conditions, structural phase transition could be realized in TMDCs, either locally or entirely. The properties of TMDCs could be dramatically changed after phase transition, e.g. a transition from the semiconducting (2H) to metallic (1T or 1T′) phase of TMDCs could greatly reduce the contact resistance between TMDCs and metal electrodes. The methods commonly employed for phase transformation include thermal annealing, chemical treatment, Ar plasma bombardment, strain, and laser irradiation.[37,209,212–215] The structural difference of 2H- and 1T (1T′)-phases in TMDCs is the spatial arrangement of chalcogen-atoms with trigonal prismatic coordination in the 2H-phase and octahedral (distorted octahedral) coordination in the 1T(1T′)-phase.[37,209] Through a transversal displacement of one chalcogen-plane, the 2H- and 1T-phases can be converted from one to the other.[209] Fig. 12o shows the STM image of a MoS_2 monolayer with local phase-transition, where the bright and dark regions correspond to the 2H- and 1T-phases, respectively. The STS analysis (Fig. 12p) reveals that the bright domains have a similar bandgap to the 2H-MoS_2, while the dark regions exhibit distinct metallic behavior.[209]

3.2. The modulation of optical properties through defect engineering

The optical properties of TMDCs can be effectively tuned by defect engineering. A pristine TMDC monolayer exhibits direct bandgap emission assigned to neutral or charged excitons. When defects are introduced into TMDCs by ion or electron beam irradiation, mid-gap states can be formed and strong localization appears surrounding the defects.[34,198,216] At low temperature, in addition to the neutral and charged exciton emission, there is a defect activated emission in TMDCs attributed to excitons bound to mid-gap states.[198] The main features of the bound excitons include: (1) a nonlinear laser power dependence and saturation phenomena at high laser power, (2) vanishing with increasing temperature, and (3) electrical gate dependence.[31,79,198,217] Fig. 13a shows that vacancies can be introduced into WSe_2 monolayers during the electron-beam lithography (EBL) process, and result in a strong bound exciton peak (X_b) located at $\sim$1.62 eV (Fig. 13b).[34]

Defect engineering can also be employed to tune the PL intensity of TMDCs. The vacancy defects in TMDCs would result in n- or p-doping and nonradiative recombination, and hence reduce the PL quantum yield. For example, MoS_2 monolayers commonly show very weak PL due to n-doping caused by S vacancies and the formation of negative trions (Fig. 3d). The vacancy defects can be healed by chemical treatment, such as with nonoxidizing acids poly(4-styrenesulfonate) (PSS) and hydrohalic acid. With the decrease of electron concentration after defect healing, the neutral excitons recombine rather than form negative trions, leading to a strong enhancement of PL intensity.[218] In addition, strong enhancement of PL can also be realized by introducing adatom defects into TMDCs, which can be realized by thermal treatment or oxygen plasma irradiation. Fig. 13c–h give PL intensity images of the as-prepared MoS_2 monolayer, and the sample annealed at 350 and 500 °C ($\sim$0.1 Pa), and after vacuum pumping, respectively.[28] According to the images and spectra (Fig. 13i), the PL of MoS_2 is greatly enhanced after annealing at both temperatures, with the 500 °C annealed sample showing stronger enhancement. The PL enhancement could be attributed to physisorption and chemisorption of oxygen (Fig. 13j and k), corresponding to samples after 350 and 500 °C annealing, respectively. Such enhancement is partially due to the charge (electron) transfer from MoS_2 to oxygen, and hence the conversion from trion to exciton emission. However, the physisorption of an oxygen molecule (350 °C annealed sample) is not stable due to the weak bonding energy, and the PL intensity is reduced after vacuum pumping. On the other hand, the PL intensity of the 500 °C annealed sample only drops slightly after vacuum pumping, indicating strong interaction between MoS_2 and the chemically adsorbed oxygen molecules. Another reason for the strong PL enhancement is the suppression of nonradiative recombination of excitons in the MoS_2 monolayer at defect sites due to the strong localization of excitons.[28] Isoelectronic substitution can also cause PL enhancement, which is due to the suppression of chalcogen defects and deep levels in the TMDC monolayer.[219] For example, the PL intensity of the $Mo_{0.82}W_{0.18}Se_2$ monolayer is $\sim$10 times stronger than that of $MoSe_2$. According to the theoretical calculations, the defect levels become closer to the CBM in $Mo_{1-x}W_xSe_2$. The concentration of Se vacancies is also suppressed in $Mo_{1-x}W_xSe_2$ due to stronger W–Se bonding, resulting in a decrease in nonradiative recombination and a longer exciton lifetime than that of pure $MoSe_2$.[219]

Tunable PL emission can be realized by isoelectronic substitution in TMDCs.[35,36,204] The monolayers of MoS_2, WS_2, $MoSe_2$ and WSe_2 possess optical bandgaps of $\sim$1.85, $\sim$1.95, $\sim$1.55, and $\sim$1.65 eV, respectively. By changing the composition of alloys, a tunable optical bandgap is achieved, such as 1.62–1.84 eV for $Mo_{1-x}W_xS_{2x}Se_{2(1-x)}$ and 1.82–1.99 eV for $Mo_{1-x}W_xS_2$, respectively.[35,204] Fig. 13l and m show the atomic structure

This journal is © The Royal Society of Chemistry 2018

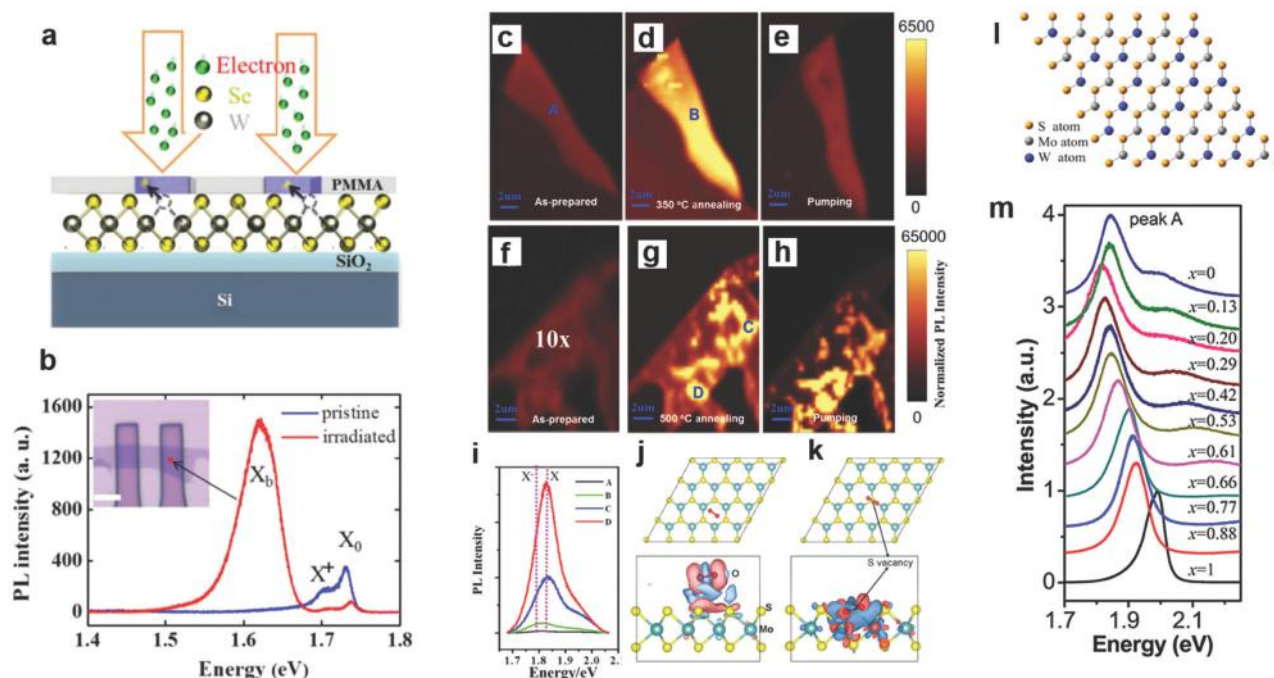Chem. Soc. Rev., 2018, 47, 3100–3128 | 3115

Fig. 13 (a) Schematic diagram of electron beam irradiation on a monolayer WSe$_2$ sample during the EBL process. (b) PL spectra of pristine monolayer WSe$_2$ and the sample after electron beam irradiation. (c–h) PL intensity images of monolayer MoS$_2$: (c and f) as-prepared, (d and g) annealed under vacuum at 350 °C and 500 °C, (e and h) after vacuum pumping. (i) PL spectra taken from locations A–D in (c–h). (j and k) Relaxed configuration and charge density difference of an O$_2$ molecule physisorbed on perfect monolayer MoS$_2$ (j) and chemisorbed on defective monolayer MoS$_2$ (k). (l) Structure of an Mo$_{1-x}$W$_x$S$_2$ monolayer. (m) PL spectra of Mo$_{1-x}$W$_x$S$_2$ monolayers with different W compositions. Reprinted with permission from: (a and b) ref. 34, Copyright 2016, Tsinghua University Press and Springer-Verlag Berlin Heidelberg; (c–k) ref. 28, Copyright 2014, American Chemical Society; (l and m) ref. 204, Copyright 2013, American Chemical Society.

and composition-dependent PL emission of Mo$_{1-x}$W$_x$S$_2$.[204] It is worth mentioning that the bandgap of the alloy shows a bowing effect,[35,204] *i.e.* the bandgap emission energy of the alloy monolayer is smaller than the linear combination of those of the initial components. Taking an Mo$_{1-x}$W$_x$S$_2$ monolayer as an example, the bandgap emission energy bowing can be described by $E_{PL,Mo_{1-x}W_xS_2} = (1-x)E_{PL,MS_2} + xE_{PL,WS_2} - bx(1-x)$, where b is the bowing parameter.[192] An Mo$_{1-x}$W$_x$S$_2$ monolayer shows a bowing parameter of 0.25 ± 0.04 eV for the A exciton and 0.19 ± 0.06 eV for the B exciton, indicating a weak bowing in composition-dependent valence band spin–orbit coupling. In addition, though WTe$_2$ is commonly 1T$'$ metallic phase, tunable bandgap PL emission can be realized in WSe$_{2(1-x)}$Te$_{2x}$ semiconductors by isoelectronic substitution of Te with Se atoms.[220]

3.3. Defect engineering for electronic devices

The properties of TMDC electronic devices are affected by various factors, such as the interface, dielectric materials, structural defects, carrier concentration and contact resistance.[136,221,222] Defect engineering provides a logical route to tune the properties of TMDC-based electronic devices through the healing of structural defects, changing the doping concentration or carrier types, and reducing contact resistance.[136,221,223]

3.3.1. Defect healing. As mentioned in Section 2.3, defects in TMDC crystals are another scattering source that greatly limits the charge carrier mobility.[136] High resolution TEM characterization reveals a large number of vacancy defects in

the TMDC monolayer, leading to a dominant hopping mechanism of charge transport at low carrier density.[32] Studies have also shown that structural defects are introduced in WSe$_2$ devices during the EBL process, and greatly degrade the hole conduction performance.[34] A monolayer WSe$_2$ device with a limited number of defects was prepared by adopting an electron-beam-free transfer-electrode technique and a maximum field-effect hole-mobility of $\sim$200 cm^2 V^{-1} s^{-1} at room temperature was achieved due to the reduced scattering sources.[34] Some chemical approaches have been employed to repair vacancy defects in TMDCs to improve the electronic performance of the devices.[136,224] Fig. 14a and b respectively show TEM images of MoS$_2$ monolayers before and after low-temperature thiol chemistry treatment, indicating the significant reduction of S vacancies.[136] The single-side and double-side healed samples show improved conductivity compared with the as-exfoliated sample, and a high mobility $>$80 cm^2 V^{-1} s^{-1} is achieved for backgated monolayer MoS$_2$ FETs (Fig. 14c). The improved mobility of the MoS$_2$ device is attributed to the significant reduction of the S vacancies, charged impurities and traps.

Apart from defect healing by chemical approaches, S vacancy self-healing (SVSH) has been reported by PSS treatment for a CVD MoS$_2$ monolayer.[218] During the SVSH treatment, the hydrogenation of PSS would guide S adatom clusters on the MoS$_2$ surface to heal the vacancies (Fig. 14d).[218] A current decrease can be observed in the output characteristic curve and the threshold voltage dramatically shifted toward zero after SVSH (Fig. 14e),

3116 | *Chem. Soc. Rev.*, 2018, **47**, 3100–3128

This journal is © The Royal Society of Chemistry 2018

indicating the decrease of electron concentration. Similar to vacancy healing *via* thiol chemistry,[136] interface trapping states of the SVSH sample are reduced according to the improvement of the subthreshold slope. The WF of the as-grown and self-healed MoS_2 is $\sim$4.3 and $\sim$4.55 eV, respectively, as revealed by ultraviolet photoelectron spectroscopy (UPS) measurement. A lateral homojunction of the MoS_2 monolayer can then be fabricated by a selected-area SVSH process and an SB height of $\sim$150 meV is obtained at the boundary. Foreign atoms can also be applied for repairing defects in TMDCs. Chalcogen vacancies in TMDCs can be healed by isoelectronic substitutional defects and the improvement of electronic properties is achieved.[224,225] A focused laser beam treatment in air has been used for healing a WSe_2 monolayer and the conductivity is enhanced by $\sim$400 times. Fig. 14f gives the output characteristics of a WSe_2 monolayer device before and after laser modification. According to the calculated band structures (Fig. 14g), defect-related mid-gap states are suppressed by substitutional oxygen at selenium vacancies.[224]

3.3.2. Controlling the carrier type and concentration. Defect engineering can also be used to control the carrier concentration in TMDCs. Studies have shown different positions of MoS_2 samples can exhibit n-type or p-type conduction, which is defect-chemistry-related and accompanied by S or Mo vacancies, respectively.[222] A mild plasma treatment (He or H_2) is used to introduce chalcogen (Se) vacancies into WSe_2 and induce n-doping.[226] The plasma treated sample shows a reduction of the metal contact resistance, a 20 times improvement in ON current and a near ideal subthreshold swing value of 66 mV dec^{-1} (Fig. 15a). On the other hand, the hole

conduction is suppressed by two orders of magnitude for the H_2-plasma treated sample.[226]

Substitutional or physisorbed impurities can be used for tuning the doping type and fabricating p–n junctions.[227] p-Type MoS_2 is prepared by a phosphorus plasma immersion ion implantation (PIII) process.[221] A large number of S vacancies in the intrinsic n-type MoS_2 facilitate the phosphorus doping.[221] Theoretical calculation confirms that the p-type doping is attributed to charge transfer originating from the substitutional and physisorbed P atoms in the top few layers of MoS_2. A lateral homogeneous p–n junction was fabricated by using area selective doping and a high rectification ratio (2×10^4) was obtained as shown in Fig. 15b.[221] p-Type doping of MoS_2 can also be realized by N_2 plasma surface treatment because of the substitution of S by N atoms.[207]

Since isoelectronic substitution doping can be realized in TMDCs by CVD growth, $WS_{2x}Se_{2-2x}$ alloys with tunable electronic properties are prepared.[36] Fig. 15c show PL spectra of $WS_{2x}Se_{2-2x}$ alloys as a function of composition. Electrical transport studies (Fig. 15c) reveal that the variation of alloy composition can tune the charge carrier types, threshold voltages, and mobility of the alloy. The doping type of a $WS_{2x}Se_{2-2x}$ alloy changes from p- to n-type with the change of the S and Se atomic ratio.[36] A lateral p–n heterojunction can also be obtained by controlling the growth of the heterojunction.[218] Since WSe_2 is intrinsically p-type and WS_2 is intrinsically n-type, the as grown WSe_2–WS_2 lateral heterojunction exhibits a rectification ratio up to 10^5 (Fig. 15d).[218]

3.3.3. Lowering contact resistance. Achieving low resistance contacts is vital for TMDC based electronic devices. The commonly used methods to reduce contact resistance by defect engineering
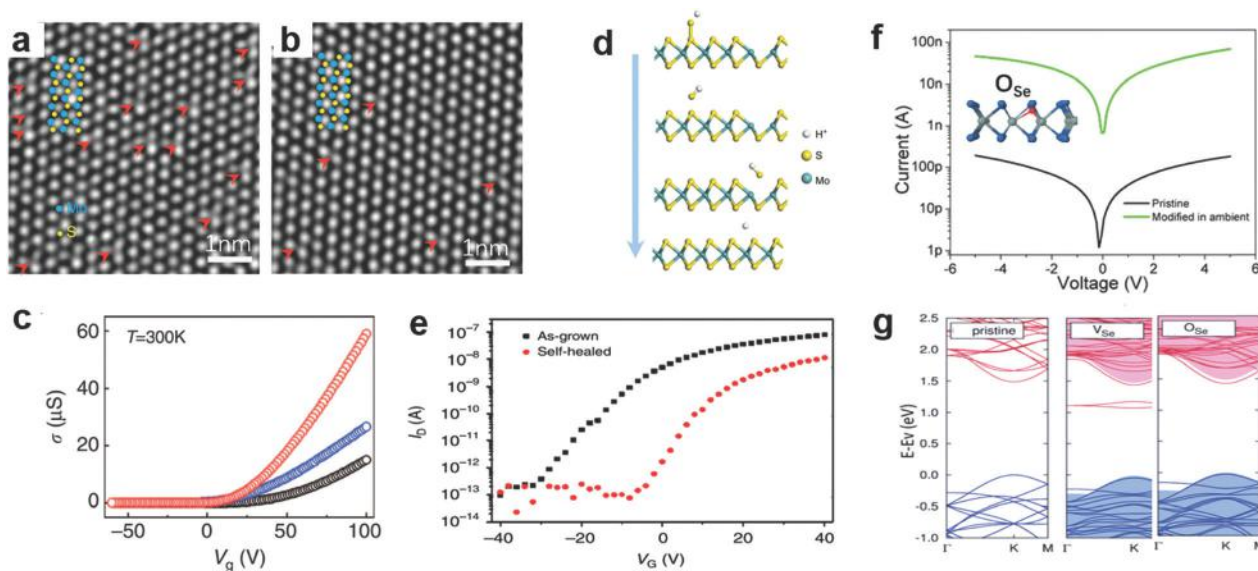

Fig. 14 (a and b) TEM images of the as-exfoliated (a) and single-side thiol chemistry treated (b) monolayer MoS_2 sample. (c) Transfer characteristics for the as-exfoliated (black), single-side treated (blue) and double-side treated (red) monolayer MoS_2. (d) Schematic diagram of SVSH in MoS_2. (e) Transfer characteristics of a monolayer MoS_2 transistor before and after SVSH. (f) Output characteristics of a monolayer WSe_2 device before and after laser modification. (g) Band structures of WSe_2: pristine WSe_2, with selenium vacancy (V_{Se}) and with oxygen replacing Se (O_{Se}). Reprinted with permission from: (a–c) Reproduced with permission from ref. 136, Copyright 2014, Nature Publishing group; (d and e) ref. 218, Copyright 2017, Nature Publishing group; (f and g) ref. 224, Copyright 2015, American Chemical Society.
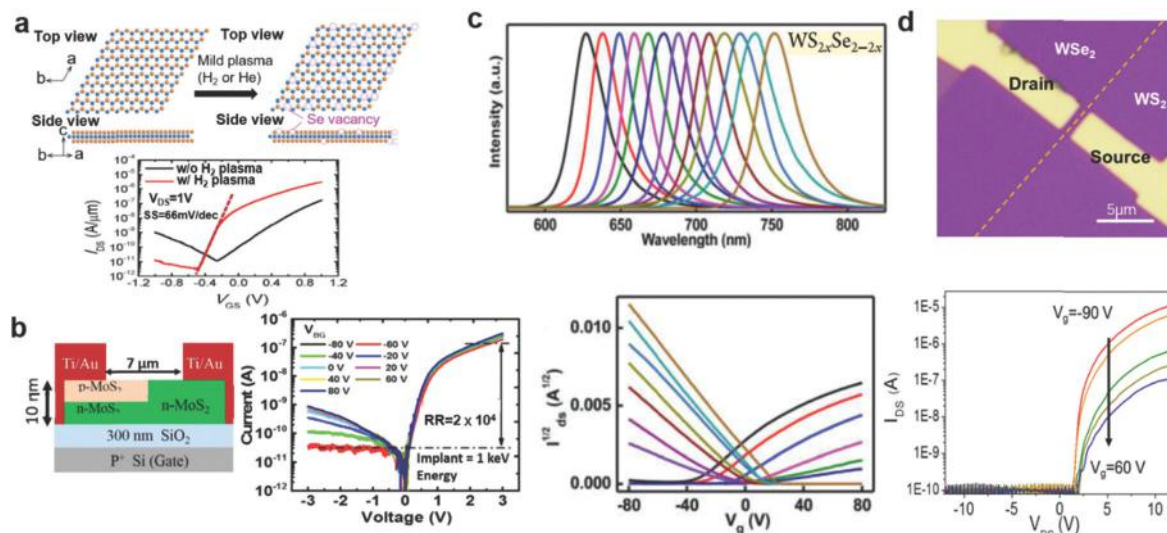
This journal is © The Royal Society of Chemistry 2018

Chem. Soc. Rev., 2018, **47**, 3100–3128 | **3117**

Fig. 15 (a) Schematic diagram of the as-exfoliated and H_2 plasma treated WSe_2, and transfer characteristics of the as-exfoliated and H_2 plasma treated WSe_2 device. (b) Schematic diagram and output characteristics of the p–n junction device of multilayer MoS_2 fabricated by area selective PIII doping. (c) PL spectra and transfer characteristics of composition tunable $WS_{2x}Se_{2-2x}$ monolayer nanosheets. (d) Optical image and output characteristics of the lateral WSe_2–WS_2 heterojunction device. Reprinted with permission from: (a) ref. 226, Copyright 2016, American Chemical Society; (b) ref. 221, Copyright 2016, American Chemical Society; (c) ref. 36, Copyright 2015, American Chemical Society; (d) ref. 208, Copyright 2017, American Association for the Advancement of Science.

include the introduction of vacancy defects, substitution doping, and local phase transition. S vacancy defects in n-type MoS_2 have been verified to dominate the metal/MoS_2 contact resistance.[222] Surface oxidation is a general approach for enhancing the performance of TMDC electronic devices. When WSe_2 is exposed to ozone (O_3) below 100 °C, tungsten oxide is formed, nucleated from edges and defects on the surface.[228] With further exposure to O_3, the oxides grow electively along selenium zigzag-edge orientations, until the top layer is fully oxidized.[228] The top oxide film blocks vertical diffusion of oxygen into the underlying WSe_2 layers, indicating that the oxidation of WSe_2 is self-limiting.[229] Electrons transfer from the underlying WSe_2 to the tungsten oxides (WO_x), resulting in highly p-doped WO_x-covered WSe_2 and a low contact barrier. The performance of WO_x-covered WSe_2 transistors has been greatly improved (Fig. 16a), showing better on-current, on/off current ratio, and carrier mobility than that of the pristine WSe_2.[223] Air heating can also improve the device performance of WSe_2 because of the formation of the in-plane heterojunction of WSe_2 and nonstoichiometric tungsten oxide (WO_{3-x}).[230] Two mechanisms can explain the improvement of performance, including (i) WO_{3-x} dopes WSe_2 and increases the hole concentration, and (ii) the highly conductive WO_{3-x} domains in WSe_2 reduce the effective channel lengths of the device, resulting in an increase in on-state current and carrier mobility.

Metallic 1T/1T′ phase TMDCs can also decrease the contact resistance of FETs and significantly improve the device performance. The local phase transition from 2H to 1T/1T′ phase can be realized by n-BuLi treatment, laser irradiation, Ar-plasma bombardment and strain.[37,209,212–215] The phase transition process by n-BuLi treatment comprises the following steps: (1) during the exposure to n-BuLi, lithium will intercalate into

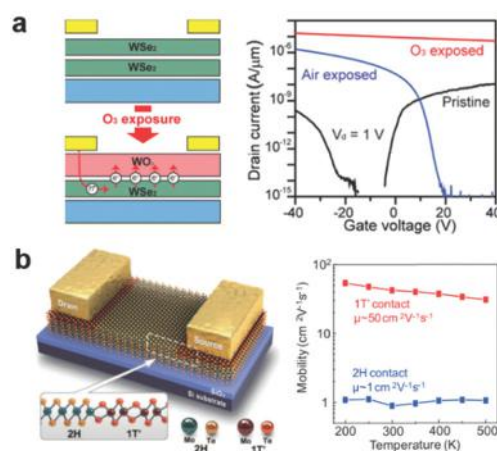Fig. 16 (a) Schematics and transfer characteristics of a WSe_2 transistor before and after O_3 exposure, and that after air exposure. (b) Schematic diagrams of a $MoTe_2$ device with a 1T′/2H phase homojunction, and field-effect mobility as a function of temperature. Reprinted with permission from: (a) ref. 223. Copyright 2016, American Chemical Society; (b) ref. 37, Copyright 2016, American Association for the Advancement of Science.

2H phase TMDCs and donate negative charges, (2) to accommodate this additional negative charge, a local transformation of the TMDCs will occur, leading to a structural change of the pristine 2H TMDCs to 1T TMDCs.[212] Phase transition of $MoTe_2$ induced by laser irradiation can be used to prepare a homojunction transistor with Ohmic contact, and increases the carrier mobility by about 50 times, while retaining a high on/off ratio of 10^6.[37] Fig. 16b gives a schematic diagram of a device constructed by 2H and 1T′ $MoTe_2$ and the field-effect mobility as a function of temperature.[37] According to the theoretical calculations and TEM characterization, the local phase transition

3118 | Chem. Soc. Rev., 2018, 47, 3100–3128

This journal is © The Royal Society of Chemistry 2018

in MoTe$_2$ is triggered by Te vacancies. A Te monovacancy concentration exceeding 3% causes the 1T′ phase to be more stable than the 2H phase.[37] Similarly, the 2H to 1T phase transition in MoS$_2$ can also be induced by Ar-plasma bombardment, which produces S vacancies and stabilizes the phase transitions.[209] Tensile strain can also be used to induce phase transition of MoTe$_2$ at room temperature, which is attributed to the reduction of the activation energy of the phase transition and results in a lowered phase transition temperature.[218] In particular, the phase transition produced by n-BuLi and tensile strain is proved to be reversible, where a 1T metallic phase can be easily converted to a 2H semiconducting phase.[214] On the other hand, the phase transition created by laser irradiation is irreversible.[37]

3.4. Defect engineering for optoelectronic devices

TMDCs with tunable bandgaps in the visible to NIR regions have attracted much interest for applications in photodetection, photovoltaics and LEDs. There is a large variation in the performance of TMDC optoelectronic devices due to different factors, such as the interface, impurities, structural defects, and the metal–semiconductor contact. Taking a MoS$_2$ photodetector as an example, the photoresponsivity varies from $\sim 10^{-5}$ to $\sim 10^4$ A W^{-1} and the response time ranges from microseconds to seconds.[2,16,231–235] Defect engineering can be applied to effectively improve the responsivity, speed and operation wavelength of photodetectors, and obtain novel photovoltaic devices and LEDs.

3.4.1. Photoconductors.
The photoconductor geometry (metal–semiconductor–metal device configuration) is mostly adopted in TMDC photodetectors. In photoconductors, photo-induced carriers increase the conductivity of semiconductors, described as the photoconductive effect.[16] In particular, there is a photoconductive gain, which is the number of charge carriers passing between the electrodes per second for each photon absorbed per second.[236] When a hole (electron) is trapped by defects, charge impurities etc.,[237,238] the electron (hole) will be replenished from the source as soon as it reaches the drain, in order to maintain charge neutrality. The multiple circulations of the electron (hole) following a single electron–hole photogeneration would lead to the high gain of the photoconductor. The photoconductive gain can then be expressed as the ratio of the free lifetime of a charge carrier to the time required for the carrier to move between the electrodes (transit time). The responsivity and response time are two important figures of merit for photoconductors, which are dominated by trapping and recombination centers. Defects can either act as trapping or recombination centers, depending on the energy levels of the defect states.[156,239,240]

The density of states (left) and simplified energy band diagram (right) of MoS$_2$ are shown in Fig. 17a.[156] There are shallow traps and deep nonradiative recombination centers existing in TMDCs, which dominate photoconductive gain. τ_r^{-1} is the nonradiative recombination rate. τ_t^{-1}, and τ_g^{-1} are the trapping and escape rate of holes into and from shallow traps, respectively. Photoresponsivity can be obtained through the following equation:

$$R = \eta \frac{\lambda q}{hc} \cdot \frac{\tau_{eff}}{\tau_{tr}},$$
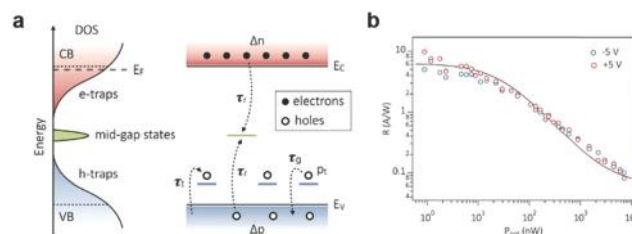

Fig. 17 (a) Schematic diagrams of the density-of-states (DOS) (left) and simplified energy band diagram of MoS$_2$ (right) that shows the main features of the charge trapping model. (b) Power dependence of photoresponsivity of the MoS$_2$ photoconductor. Reprinted with permission from ref. 156, Copyright 2014, American Chemical Society.

where $\tau_{eff} = \tau_r(\tau_g/\tau_t)$ is the effective carrier lifetime, $\tau_{tr} = L^2/(\mu_n V_D)$ is the electron transit time through the device,[156] and $\frac{\tau_{eff}}{\tau_{tr}}$ is the photoconductive gain. According to the above analysis, high responsivity of TMDCs can be realized by increasing shallow traps and reducing deep nonradiative recombination. Fig. 17b shows the power dependence of the photoresponsivity of a MoS$_2$ photoconductor.[156] From theoretical calculation, the responsivity of MoS$_2$ in trap-free conditions is only about 0.06 A W^{-1}, which is much smaller than the experimentally observed value of ~ 6 A W^{-1}. The high responsivity of MoS$_2$ is attributed to the large number of shallow trapping centers. According to the fitting of the experimental data in Fig. 17b, the effective energetic position of the traps is ~ 0.27 eV above the valence band edge. On the other hand, due to the limited number of defects/traps in the highly crystalline MoSe$_2$ samples synthesized by CVD, the MoSe$_2$ photoconductor presents much lower responsivity as compared to the MoS$_2$ device.[241] One piece of evidence is that the low temperature PL spectrum of MoS$_2$ shows a strong defect-activated PL peak (X$_b$) arising from excitons binding to defect states, while such a peak is absent in MoSe$_2$.[241] The photoresponsivity of the WSe$_2$ monolayer can be improved by ~ 150 times by laser modification,[224] due to the introduction of oxygen-related defects. Moreover, the photoresponsivity of few-layer rhenium disulfide (ReS$_2$) can reach as high as 88 600 A W^{-1}, attributed to the increased light absorption by the multilayer as well as the gain enhancement due to the existence of trap states.[159] However, the achieved ultrahigh gain is always accompanied by an increased response time, which is normally in the time scale of seconds for ReS$_2$ photoconductors. The photoconductivity can also be enhanced in alloys (e.g. WS$_{2(1-x)}$Se$_{2x}$), which is attributed to the carrier diffusion and confinement into the alloy region according to finite element analysis.[242]

The factor that affects the response time in TMDC photoconductors is the carrier recombination. An ultrafast two-pulse photovoltage correlation (TPPC) technique (Fig. 18a), which offers carrier recombination dynamics, has been employed on a monolayer MoS$_2$ photodetector (Fig. 18b) to obtain the intrinsic response times.[243] Two pulses of 452 nm (2.74 eV, ~ 150 fs) with a time delay of Δt are focused on the metal–MoS$_2$ junction (Fig. 18b). The electrons and holes are separated by the lateral electrical field of the junction. The photoresponse
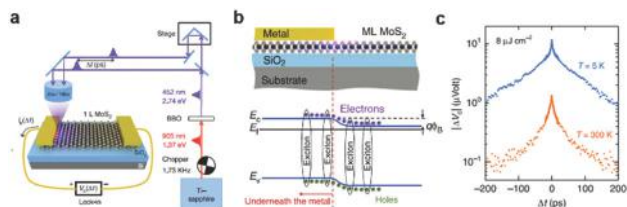
This journal is © The Royal Society of Chemistry 2018

Chem. Soc. Rev., 2018, 47, 3100–3128 | 3119

Fig. 18 (a) A schematic of the TPPC experiment. (b) The energy band diagram of the metal−MoS$_2$ junction after photoexcitation with an optical pulse. (c) TPPC signals $V_c(\Delta t)$ as a function of the time delay Δt between the pulses measured at 5 and 300 K, respectively. The plot shows two time-scales: a fast timescale of ~4.3 ps, and a slow timescale of ~105 ps, which are largely temperature independent. Reprinted with permission from ref. 243, Copyright 2015, Nature Publishing Group.

varied with Δt as measured by a lock-in amplifier. Photovoltage $V_c(\Delta t)$ as a function of the time delay Δt between the two pulses is shown in Fig. 18c. $\Delta V_c(\Delta t)$, defined as $V_c(\Delta t) - V_c(\infty)$, shows a fast timescale of ~4.3 ps and a slow timescale of ~105 ps, which are independent of the temperature. As theoretically proposed, carriers are captured by one fast and one slow defect level *via* Auger scattering,[244] where the Auger process means that an exciton is annihilated at a defect site with the capture of the electron (or the hole) by the defect and the hole (or the electron) is scattered to a high energy. Most of the photoexcited holes (both free and bound) and electrons are captured by the fast defects within the first few picoseconds after photoexcitation and only a small fraction is captured by the slow defects. The photoexcited carriers recombine or are captured by defects in the few picoseconds range, resulting in a fast response time and a low internal quantum efficiency.[244–248]

Since defects can also act as recombination centers to determine the response time, one can control the types and density of defects in TMDCs to achieve fast photodetection. Fast temporal response of the ReS$_2$ photoconductor can be obtained by O$_2$ plasma treatment.[249] O$_2$ plasma treatment creates trap states in the bandgap of ReS$_2$, which would increase the recombination rate of the photocarriers, and consequently reduce the photocarrier lifetime and response time (rise time of 670 ms).[249] Since the absorbance of ReS$_2$ is saturated above 10 nm, the photoresponsivity is still high for the plasma treated ReS$_2$ with the thickness of ~30 nm.[249] When both fast and slow recombination centers are presented in CVD-grown monolayer MoS$_{2(1-x)}$Se$_{2x}$ alloy devices, a superlinear photocurrent is observed. A superlinear photocurrent emerges when the nonequilibrium occupancy of initially empty fast recombination centers becomes comparable to that of slow recombination centers.[250] During illumination, the free hole and electron concentrations increase, and their respective quasi Fermi levels move closer to the valence and conduction band edges. At a high intensity of illumination, the initially empty centers near the conduction band become partially filled, and the recombination rate drops rapidly, which signals the onset of superlinearity.[250]

The wavelength range or bandwidth of the photoresponse is another key factor for photodetection. The range of light absorption is varied for different TMDCs due to different
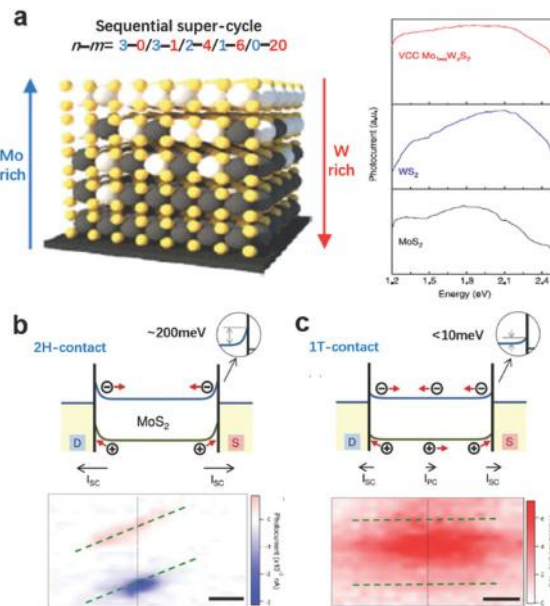

Fig. 19 (a) Sequential super-cycle ALD procedure and schematic structure of a VCC Mo$_{1-x}$W$_x$S$_2$ multilayer (left) and spectral photocurrent of a VCC Mo$_{1-x}$W$_x$S$_2$ multilayer, and 5l WS$_2$ and 5l MoS$_2$ photodetectors (right). Proposed mechanisms of photocurrent generation at zero gate bias and scanning photocurrent microscopy in (b) 2H-contacted and (c) 1T-contacted devices, respectively. Reprinted with permission from: (a) ref. 251, Copyright 2015, Nature Publishing Group; (b and c) ref. 252, Copyright 2015, American Chemical Society.

electronic bandgaps. TMDC alloys with tunable bandgaps show promising potential for broadband optoelectronic applications. A vertically composition-controlled (VCC) Mo$_{1-x}$W$_x$S$_2$ multilayer has been synthesized by using sulphurization of Mo$_{1-x}$W$_x$O$_y$ (Fig. 19a)[251] grown *via* super-cycle atomic layer deposition. The VCC Mo$_{1-x}$W$_x$S$_2$ multilayer with strong interlayer coupling has different vertical composition and broadband light absorption, resulting in a 3–4 times greater photocurrent than that of MoS$_2$- and WS$_2$-based devices (Fig. 19a). The VCC Mo$_{1-x}$W$_x$S$_2$ multilayer has a broadband photocurrent from 1.2 to 2.5 eV, which is broader than 1.3 and 2.1 eV for a WS$_2$ multilayer and 1.2 and 1.8 eV for an MoS$_2$ multilayer.[251]

Low contact resistance is essential to obtain intrinsic and high-performance photodetection. Local phase transition underneath the metal electrodes is realized in TMDC optoelectronic devices and the photoresponsivity is enhanced by more than an order of magnitude due to the reduction of SB.[252] The SB heights of 1T- and 2H-contacted MoS$_2$ devices are a few meV and ~200 meV, respectively (Fig. 19b and c).[252] The maximum photocurrent is generated at the contacts for 2H-phase MoS$_2$, while the photocurrent peak of the sample with 1T-phase contacts is at the device channel (Fig. 19b and c). Under a bias, the photocurrent of a 2H device is greatly affected by the high SB. However, the photocurrent of 1T devices is mainly attributed to the intrinsic photoresponse because of the low SB at both contacts. Other approaches employed for reducing contact resistance, such as substitution doping and adsorption, can also be applied to improve the optoelectronic performances of TMDCs.
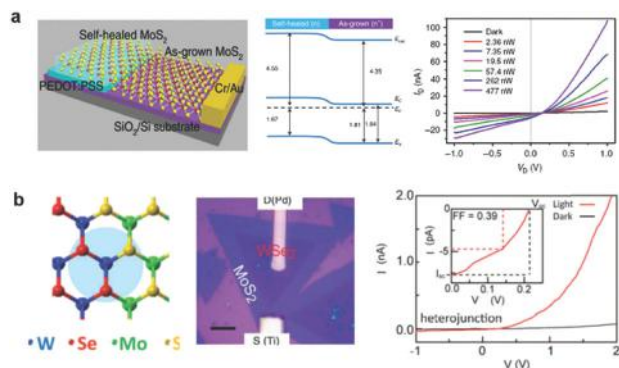
3120 | *Chem. Soc. Rev.*, 2018, **47**, 3100–3128

This journal is © The Royal Society of Chemistry 2018

Fig. 20 (a) Schematic diagram, band diagram and photovoltaic effect under different illumination intensities (575 nm) of the monolayer MoS_2 homojunction by selective area S vacancy self-healing. (b) Atomic model, optical image, and output characteristics with and without light exposure of a WSe_2–MoS_2 lateral heterostructure. Reprinted with permission from: (a) ref. 218, Copyright 2017, Nature Publishing Group; ref. 255, Copyright 2015, American Association for the Advancement of Science.

3.4.2. Photovoltaics. Photovoltaic device can be constructed by partially healing the defects in TMDCs. The S vacancies in MoS_2 can be healed by PSS treatment and a homojunction is constructed by selective area S vacancy self-healing (Fig. 20a).[218] Fig. 20a gives the band diagram of the monolayer MoS_2 homojunction with a SB height of ~ 150 meV for the as-grown and self-healed regions. The photoresponse at the homojunction as a function of light intensity is shown in Fig. 20a. An excellent responsivity of ~ 308 mA W^{-1} at zero bias is obtained due to the photovoltaic effect, which has a much faster response time than that of the MoS_2-based photoconductors.[2,16,253]

Recently, to achieve a high-performance monolayer photovoltaic device, a lateral TMDC heterojunction was constructed by two-step epitaxial growth.[254,255] For example, a WSe_2–MoS_2 lateral p–n junction shows an atomically sharp interface (atomic model shown in Fig. 20b) and offers band offset tuning.[254] Asymmetric metal contacts, Pd and Ti/Au, are deposited on p-type WSe_2 and n-type MoS_2, respectively. The I–V characteristic curve of the junction exhibits good rectification character.[255] A photovoltaic effect with an open-circuit voltage of 0.22 V and a short-circuit current of 7.7 pA is achieved under light illumination (power density of 1 mW cm^{-2}). The extracted fill factor (FF) and the calculated power conversion efficiency (PCE) are 0.39 and 0.2%, respectively. The highest PCE reported is 2.56% due to the high quality atomically sharp interface.[254] In addition, the PCE of the lateral heterojunction has small dependence on the angles of incidence (AOIs) with merely 5% loss of PCE at an AOI of 75°.[254] This is superior as compared to Si-based solar cells, which show 90% PCE reduction from 0° to 75° AOI.[256] On the other hand, the efficiency of a photovoltaic device based on a vertically stacked TMDC heterostructure is limited by quenching centers, such as contaminants and defects at the interface, or corrugations at the surface.[198,257,258]

3.4.3. Electroluminescence. When suitably isolated, defects can act as single quantum emitters (SQEs) in TMDCs. If SQEs are incorporated into LEDs, quantum LEDs can be fabricated with great potential for quantum information and technology applications. Quantum LEDs can be realized by vertical stacking of layered materials and charge can be injected into the active layer containing quantum emitters, *i.e.* defect sites.[259] Fig. 21a shows a quantum LED including a single layer of graphene (SLG), a thin (2–6 atomic layers) sheet of hexagonal boron nitride (h-BN)
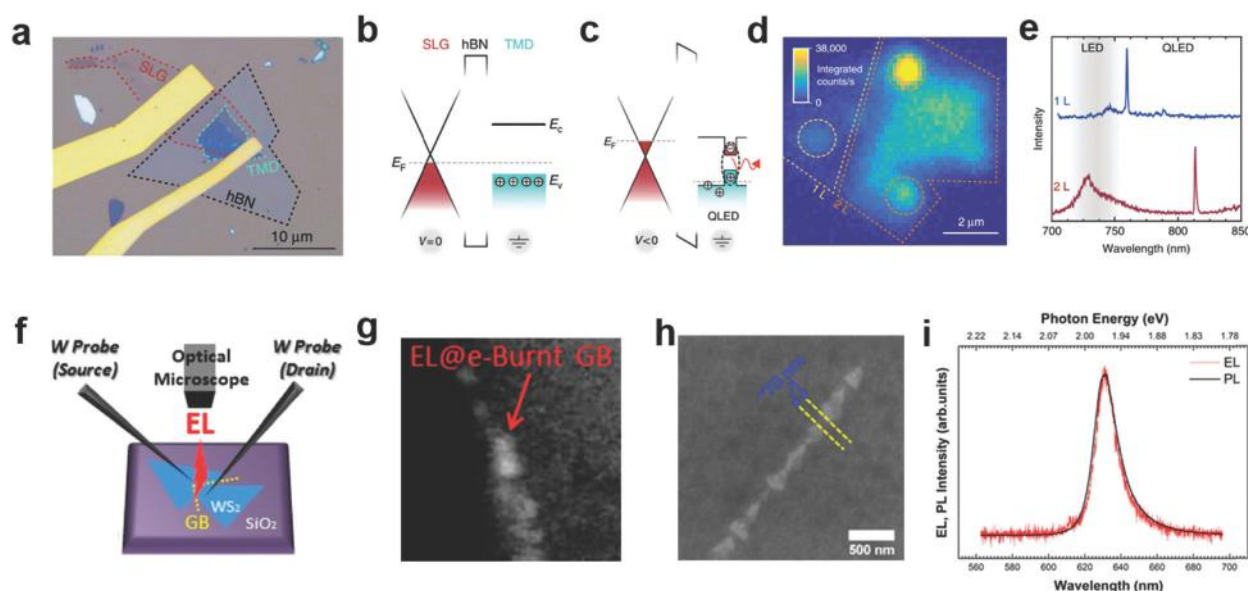

Fig. 21 (a) Optical image, (b and c) heterostructure band diagram, (d) EL intensity map, and (e) EL emission spectra of a TMDC based quantum LED. (f) Schematic illustration of the experimental setup used for generating EL in a GB region of a WS_2 sample. (g) Red-channel only optical image of EL localized in an eroded GB. (h) SEM images of monolayer-WS_2 nanoribbons at GB regions after partial erosion. (i) Normalized EL and PL spectra of a WS_2 monolayer device with GBs. Reprinted with permission from: (a–e) ref. 259, Copyright 2016, Nature Publishing Group; (f–i) ref. 261, Copyright 2015, American Chemical Society.

This journal is © The Royal Society of Chemistry 2018

Chem. Soc. Rev., 2018, **47**, 3100–3128 | 3121

and a mono- or bi-layer of TMDC, such as WSe_2, to form a p-i-n junction. Fig. 21b and c show the operational concept of the TMDC-LED, indicating that charge flow is prevented between the layers at zero bias (Fig. 21b) and electrons tunnel from the SLG into the WSe_2 monolayer through the h-BN tunnel barrier at a negative bias (Fig. 21c), and finally radiatively recombine. Localized states introduced by defects lie in the bandgap of WSe_2 and excitons localized by these states emit at lower energies compared with free exciton emission.[200,201,204] Fig. 21d shows a spatial map of the integrated electroluminescence (EL) from a WSe_2-based LED. In addition to light emission from free excitons, quantum emissions from localized light emission are observed in the WSe_2 monolayers and bilayers shown in the dotted circles of Fig. 21d. The typical EL emission spectra of WSe_2 monolayers and bilayers show quantum emissions with linewidths ranging between 0.8 and 3 nm (Fig. 21e). In addition to the structure of SLG/h-BN/TMDC, other p-i-n junctions can also be constructed to obtain quantum LEDs. For example, the SLG/h-BN/TMDC/h-BN/SLG structure has been designed, where SLG layers act as semitransparent electrodes, the TMDC offers radiation recombination centers and h-BN act as a tunnel barrier.[260] When the device is biased, electrons (holes) can tunnel from the negative (positive) electrode through the thin h-BN barriers to defect states in the WSe_2 layer, resulting in recombination of excitons and hence producing EL.[260] Single defect EL is detected by adopting a confocal detection method using a pinhole. The EL peak is composed of a fine structure doublet with two narrow lines (width of ~ 300 μeV) separated by 0.9 meV, which is consistent with SQEs in WSe_2.[260]

Grain boundaries (GB) as typical line defects in CVD TMDCs can also influence the EL behavior. Fig. 21f shows a schematic illustration of the experimental setup used for generating EL in WS_2 domains with a GB, where ultrafine W probe tips as contacts are used to apply source–drain bias.[261] The GBs degrade after increasing V_{SD} due to the localized Joule heating induced oxidization, and strong EL could be observed at the eroded GB region (Fig. 21g). It can be seen from the SEM image in Fig. 21h that there are randomly distributed micro- and nanoribbons formed within the GB of WS_2. Restricting current to flow through the ribbons would enhance the carrier recombination rates, and hence introduce strong and localized EL at the eroded GB regions.[261] Fig. 21i shows similar EL and PL spectra, indicating that EL originates from electron–hole (exciton) recombination across the direct bandgap.

4. Conclusions and outlook

The recent progress on interface and defect engineering for 2D TMDCs towards high-performance electronic and opto-electronic devices has been reviewed. Three types of interfaces in TMDC-based devices are highlighted, including the TMDC/adsorbate, TMDC/metal contact and TMDC/dielectric interface, which can be suitably engineered by the rational choice of interface engineering schemes. Surface charge transfer doping occurring at the TMDC/adsorbate interface has been demonstrated

to be an effective method to tune the charge carrier type and concentration of 2D TMDCs, which significantly impacts both the electronic and optical properties. At TMDC/metal contact interface, several strategies like contact doping and buffer layer engineering have been utilized to lower the Schottky barrier, thus facilitating the carrier transport in TMDCs. Various extrinsic impurities existing at TMDC/dielectric interfaces can induce severe scattering of charge carriers during the transport. An appropriate dielectric engineering scheme, such as the selection of high- or low-k dielectrics, is effective to suppress the scattering, leading to a highly improved device performance. The second part on defect engineering reviews a variety of defects existing in the lattice of TMDCs, e.g. vacancies, substitutional impurities, grain boundaries, and local phase transitions, and their effects on the electronic and optical properties of TMDCs. Defect engineering has been demonstrated to efficiently modulate the optical properties of TMDCs, e.g. introducing bound exciton emission, enhancing the PL quantum efficiency and tuning the PL emission energy. Appropriate defect engineering can notably facilitate the charge carrier transport by defect healing, generating effective doping as well as lowering the contact resistance in electronic devices. Finally, defect engineering has been utilized to improve the responsivity, speed and operation wavelength of photodetectors, and realize novel photovoltaic devices and quantum LEDs.

Interface and defect engineering not only open up new research areas on tuning the fundamental properties of TMDCs, but also pave the way for the practical device applications of interface- or structure-modified TMDCs in future electronics and optoelectronics. However, there still exists much room for further improvement. For example, stable and non-toxic degenerate p-type dopants are still absent for practical device applications, and new dangling-bond-free high-k layered dielectric materials are also required to achieve an ideal TMDC/dielectric interface in TMDC devices (h-BN is a commonly used low-k dielectric). In addition, defect engineering also faces challenges, such as how to simultaneously achieve high-response and fast photoresponsivity in TMDC-based photodetectors and how to trigger single-photon EL with high efficiency in defect-engineered TMDCs. The aforementioned challenges could be overcome by precisely controlling the type and density of defects in TMDCs, and by introducing localized density states with suitable energy levels.

Conflicts of interest

There are no conflicts to declare.

Acknowledgements

3122 | Chem. Soc. Rev., 2018, 47, 3100–3128

This journal is © The Royal Society of Chemistry 2018

References

1 A. K. Geim, *Science*, 2009, **324**, 1530–1534.
2 O. Lopez-Sanchez, D. Lembke, M. Kayci, A. Radenovic and A. Kis, *Nat. Nanotechnol.*, 2013, **8**, 497–501.
3 X. Ling, H. Wang, S. Huang, F. Xia and M. S. Dresselhaus, *Proc. Natl. Acad. Sci. U. S. A.*, 2015, **112**, 4523–4530.
4 Y. Kubota, K. Watanabe, O. Tsuda and T. Taniguchi, *Science*, 2007, **317**, 932–934.
5 Q. H. Wang, K. Kalantar-Zadeh, A. Kis, J. N. Coleman and M. S. Strano, *Nat. Nanotechnol.*, 2012, **7**, 699–712.
6 J. Lu, H. Liu, E. S. Tok and C.-H. Sow, *Chem. Soc. Rev.*, 2016, **45**, 2494–2515.
7 G. R. Bhimanapati, Z. Lin, V. Meunier, Y. Jung, J. Cha, S. Das, D. Xiao, Y. Son, M. S. Strano and V. R. Cooper, *ACS Nano*, 2015, **9**, 11509–11539.
8 C. R. Ryder, J. D. Wood, S. A. Wells and M. C. Hersam, *ACS Nano*, 2016, **10**, 3900–3917.
9 H. Schmidt, F. Giustiniano and G. Eda, *Chem. Soc. Rev.*, 2015, **44**, 7715–7736.
10 C. Tan, X. Cao, X.-J. Wu, Q. He, J. Yang, X. Zhang, J. Chen, W. Zhao, S. Han and G.-H. Nam, *Chem. Rev.*, 2017, **117**, 6225–6331.
11 X. Xu, W. Yao, D. Xiao and T. F. Heinz, *Nat. Phys.*, 2014, **10**, 343–350.
12 A. Kuc, N. Zibouche and T. Heine, *Phys. Rev. B: Condens. Matter Mater. Phys.*, 2011, **83**, 245213.
13 B. Radisavljevic, A. Radenovic, J. Brivio, V. Giacometti and A. Kis, *Nat. Nanotechnol.*, 2011, **6**, 147–150.
14 H. Zeng, J. Dai, W. Yao, D. Xiao and X. Cui, *Nat. Nanotechnol.*, 2012, **7**, 490–493.
15 K. F. Mak, K. He, J. Shan and T. F. Heinz, *Nat. Nanotechnol.*, 2012, **7**, 494–498.
16 C. Xie, C. Mak, X. Tao and F. Yan, *Adv. Funct. Mater.*, 2017, **27**, 1603886.
17 L. Britnell, R. Ribeiro, A. Eckmann, R. Jalil, B. Belle, A. Mishchenko, Y.-J. Kim, R. Gorbachev, T. Georgiou and S. Morozov, *Science*, 2013, **340**, 1311–1314.
18 F. K. Perkins, A. L. Friedman, E. Cobas, P. M. Campbell, G. G. Jernigan and B. T. Jonker, *Nano Lett.*, 2013, **13**, 668–673.
19 G. H. Lee, Y. J. Yu, X. Cui, N. Petrone, C. H. Lee, M. S. Choi, D. Y. Lee, C. Lee, W. J. Yoo and K. Watanabe, *ACS Nano*, 2013, **7**, 7931–7936.
20 W. H. Wang, R. X. Du, X. T. Guo, J. Jiang, W. W. Zhao, Z. H. Ni, X. R. Wang, Y. M. You and Z. H. Ni, *Light: Sci. Appl.*, 2017, **6**, e17113.
21 X. Guo, W. Wang, H. Nan, Y. Yu, J. Jiang, W. Zhao, J. Li, Z. Zafar, N. Xiang and Z. Ni, *Optica*, 2016, **3**, 1066–1070.
22 X. Zhang, Z. Shao, X. Zhang, Y. He and J. Jie, *Adv. Mater.*, 2016, **28**, 10409–10442.
23 A. Allain, J. Kang, K. Banerjee and A. Kis, *Nat. Mater.*, 2015, **14**, 1195–1205.
24 T. Cao, G. Wang, W. Han, H. Ye, C. Zhu, J. Shi, Q. Niu, P. Tan, E. Wang and B. Liu, *Nat. Commun.*, 2012, **3**, 887.
25 M. S. Choi, D. Qu, D. Lee, X. Liu, K. Watanabe, T. Taniguchi and W. J. Yoo, *ACS Nano*, 2014, **8**, 9332–9340.

26 L. Yu, A. Zubair, E. J. Santos, X. Zhang, Y. Lin, Y. Zhang and T. S. Palacios, *Nano Lett.*, 2015, **15**, 4928–4934.
27 W. Zhou, X. Zou, S. Najmaei, Z. Liu, Y. Shi, J. Kong, J. Lou, P. M. Ajayan, B. I. Yakobson and J.-C. Idrobo, *Nano Lett.*, 2013, **13**, 2615–2622.
28 H. Nan, Z. Wang, W. Wang, Z. Liang, Y. Lu, Q. Chen, D. He, P. Tan, F. Miao, X. Wang, J. Wang and Z. Ni, *ACS Nano*, 2014, **8**, 5738–5745.
29 A. M. Van Der Zande, P. Y. Huang, D. A. Chenet, T. C. Berkelbach, Y. You, G.-H. Lee, T. F. Heinz, D. R. Reichman, D. A. Muller and J. C. Hone, *Nat. Mater.*, 2013, **12**, 554–561.
30 J. Suh, T. E. Park, D. Y. Lin, D. Fu, J. Park, H. J. Jung, Y. Chen, C. Ko, C. Jang, Y. Sun, R. Sinclair, J. Chang, S. Tongay and J. Wu, *Nano Lett.*, 2014, **14**, 6976–6982.
31 Z. Wu and Z. Ni, *Nanophotonics*, 2017, **6**, 1219–1237.
32 H. Qiu, T. Xu, Z. Wang, W. Ren, H. Nan, Z. Ni, Q. Chen, S. Yuan, F. Miao and F. Song, *Nat. Commun.*, 2013, **4**, 2642.
33 K. Kaasbjerg, K. S. Thygesen and K. W. Jacobsen, *Phys. Rev. B: Condens. Matter Mater. Phys.*, 2012, **85**, 115317.
34 Z. Wu, Z. Luo, Y. Shen, W. Zhao, W. Wang, H. Nan, X. Guo, L. Sun, X. Wang and Y. You, *Nano Res.*, 2016, **9**, 3622–3631.
35 S. Susarla, A. Kutana, J. A. Hachtel, V. Kochat, A. Apte, R. Vajtai, J. C. Idrobo, B. I. Yakobson, C. S. Tiwary and P. M. Ajayan, *Adv. Mater.*, 2017, **29**, 1702457.
36 X. Duan, C. Wang, Z. Fan, G. Hao, L. Kou, U. Halim, H. Li, X. Wu, Y. Wang and J. Jiang, *Nano Lett.*, 2016, **16**, 264–269.
37 S. Cho, S. Kim, J. H. Kim, J. Zhao, J. Seok, D. H. Keum, J. Baik, D.-H. Choe, K. Chang and K. Suenaga, *Science*, 2015, **349**, 625–628.
38 W. Chen, D. Qi, X. Gao and A. T. S. Wee, *Prog. Surf. Sci.*, 2009, **84**, 279–321.
39 H. Lüth, *Solid surfaces, interfaces and thin films*, Springer, 2001.
40 W. Chen, S. Chen, D. C. Qi, X. Y. Gao and A. T. S. Wee, *J. Am. Chem. Soc.*, 2007, **129**, 10418–10422.
41 Z. Chen, I. Santoso, R. Wang, L. F. Xie, H. Y. Mao, H. Huang, Y. Z. Wang, X. Y. Gao, Z. K. Chen and D. Ma, *Appl. Phys. Lett.*, 2010, **96**, 213104.
42 D. Xiang, C. Han, J. Wu, S. Zhong, Y. Liu, J. Lin, X.-A. Zhang, W. P. Hu, B. Özyilmaz and A. C. Neto, *Nat. Commun.*, 2015, **6**, 6485.
43 C. Han, J. Lin, D. Xiang, C. Wang, L. Wang and W. Chen, *Appl. Phys. Lett.*, 2013, **103**, 263117.
44 P. Wei, N. Liu, H. R. Lee, E. Adijanto, L. Ci, B. D. Naab, J. Q. Zhong, J. Park, W. Chen and Y. Cui, *Nano Lett.*, 2013, **13**, 1890–1897.
45 S. Zhong, J. Q. Zhong, H. Y. Mao, R. Wang, Y. Wang, D. C. Qi, K. P. Loh, A. T. S. Wee, Z. K. Chen and W. Chen, *ACS Appl. Mater. Interfaces*, 2012, **4**, 3134–3140.
46 N. Koch, S. Duhm, J. P. Rabe, A. Vollmer and R. L. Johnson, *Phys. Rev. Lett.*, 2005, **95**, 237601.
47 N. Koch, S. Duhm, J. P. Rabe, S. Rentenberger, R. L. Johnson, J. Klankermayer and F. Schreiber, *Appl. Phys. Lett.*, 2005, **87**, 101905.
48 E. L. Bruner, N. Koch, A. R. Span, S. L. Bernasek, A. Kahn and J. Schwartz, *J. Am. Chem. Soc.*, 2002, **124**, 3192–3193.

This journal is © The Royal Society of Chemistry 2018

Chem. Soc. Rev., 2018, **47**, 3100–3128 | 3123

49 H. Dong, H. Zhu, Q. Meng, X. Gong and W. Hu, *Chem. Soc. Rev.*, 2012, **41**, 1754–1808.

50 Y. Zhao, K. Xu, F. Pan, C. Zhou, F. Zhou and Y. Chai, *Adv. Funct. Mater.*, 2017, **27**, 1603484.

51 W. Lei, G. Liu, J. Zhang and M. Liu, *Chem. Soc. Rev.*, 2017, **46**, 3492–3509.

52 Z. Hu, Q. Li, B. Lei, Q. Zhou, D. Xiang, Z. Lyu, F. Hu, J. Wang, Y. Ren and R. Guo, *Angew. Chem., Int. Ed.*, 2017, **56**, 9131–9135.

53 C. Han, Z. Hu, A. Carvalho, N. Guo, J. Zhang, F. Hu, D. Xiang, J. Wu, B. Lei and L. Wang, *2D Mater.*, 2017, **4**, 021007.

54 S. P. Koenig, R. A. Doganov, L. Seixas, A. Carvalho, J. Y. Tan, K. Watanabe, T. Taniguchi, N. Yakovlev, A. H. Castro Neto and B. Özyilmaz, *Nano Lett.*, 2016, **16**, 2145–2151.

55 S. Mouri, Y. Miyauchi and K. Matsuda, *Nano Lett.*, 2013, **13**, 5944–5948.

56 D. Kiriya, M. Tosun, P. Zhao, J. S. Kang and A. Javey, *J. Am. Chem. Soc.*, 2014, **136**, 7853–7856.

57 H. Fang, M. Tosun, G. Seol, T. C. Chang, K. Takei, J. Guo and A. Javey, *Nano Lett.*, 2013, **13**, 1991–1995.

58 J. D. Lin, C. Han, F. Wang, R. Wang, D. Xiang, S. Qin, X.-A. Zhang, L. Wang, H. Zhang and A. T. S. Wee, *ACS Nano*, 2014, **8**, 5323–5329.

59 B. Lei, Z. Hu, D. Xiang, J. Wang, G. Eda, C. Han and W. Chen, *Nano Res.*, 2017, **10**, 1282–1291.

60 S. H. Jo, D. H. Kang, J. Shim, J. Jeon, M. H. Jeon, G. Yoo, J. Kim, J. Lee, G. Y. Yeom and S. Lee, *Adv. Mater.*, 2016, **28**, 4824–4831.

61 B. Liu, L. Chen, G. Liu, A. N. Abbas, M. Fathi and C. Zhou, *ACS Nano*, 2014, **8**, 5304–5314.

62 L. Yang, K. Majumdar, H. Liu, Y. Du, H. Wu, M. Hatzistergos, P. Hung, R. Tieckelmann, W. Tsai and C. Hobbs, *Nano Lett.*, 2014, **14**, 6275–6280.

63 H.-Y. Park, S. R. Dugasani, D.-H. Kang, J. Jeon, S. K. Jang, S. Lee, Y. Roh, S. H. Park and J.-H. Park, *ACS Nano*, 2014, **8**, 11603–11613.

64 C. J. Lockhart de la Rosa, A. Nourbakhsh, M. Heyne, I. Asselberghs, C. Huyghebaert, I. Radu, M. Heyns and S. De Gendt, *Nanoscale*, 2017, **9**, 258–265.

65 Y. Du, H. Liu, A. T. Neal, M. Si and D. Y. Peide, *IEEE Electron Device Lett.*, 2013, **34**, 1328–1330.

66 S. Dey, H. S. Matte, S. N. Shirodkar, U. V. Waghmare and C. N. Rao, *Chem. – Asian J.*, 2013, **8**, 1780–1784.

67 Y. Shi, J. K. Huang, L. Jin, Y. T. Hsu, S. F. Yu, L. J. Li and H. Y. Yang, *Sci. Rep.*, 2013, **3**, 1839.

68 C.-H. Chen, C.-L. Wu, J. Pu, M.-H. Chiu, P. Kumar, T. Takenobu and L.-J. Li, *2D Mater.*, 2014, **1**, 034001.

69 S. Tongay, J. Zhou, C. Ataca, J. Liu, J. S. Kang, T. S. Matthews, L. You, J. Li, J. C. Grossman and J. Wu, *Nano Lett.*, 2013, **13**, 2831–2836.

70 J. Lin, H. Li, H. Zhang and W. Chen, *Appl. Phys. Lett.*, 2013, **102**, 203109.

71 H. Fang, S. Chuang, T. C. Chang, K. Takei, T. Takahashi and A. Javey, *Nano Lett.*, 2012, **12**, 3788–3792.

72 M. Amani, D.-H. Lien, D. Kiriya, J. Xiao, A. Azcatl, J. Noh, S. R. Madhvapathy, R. Addou, K. Santosh and M. Dubey, *Science*, 2015, **350**, 1065–1068.

73 Y. Li, C.-Y. Xu, P. Hu and L. Zhen, *ACS Nano*, 2013, **7**, 7795–7804.

74 W. J. Yu, L. Liao, S. H. Chae, Y. H. Lee and X. Duan, *Nano Lett.*, 2011, **11**, 4759–4763.

75 S. M. Kim, J. H. Jang, K. K. Kim, H. K. Park, J. J. Bae, W. J. Yu, I. H. Lee, G. Kim, D. D. Loc and U. J. Kim, *J. Am. Chem. Soc.*, 2008, **131**, 327–331.

76 P. Zhao, D. Kiriya, A. Azcatl, C. Zhang, M. Tosun, Y.-S. Liu, M. Hettick, J. S. Kang, S. McDonnell and S. KC, *ACS Nano*, 2014, **8**, 10808–10814.

77 B. Chakraborty, A. Bera, D. Muthu, S. Bhowmick, U. V. Waghmare and A. Sood, *Phys. Rev. B: Condens. Matter Mater. Phys.*, 2012, **85**, 161403.

78 Z. Li, R. Ye, R. Feng, Y. Kang, X. Zhu, J. M. Tour and Z. Fang, *Adv. Mater.*, 2015, **27**, 5235–5240.

79 J. S. Ross, S. Wu, H. Yu, N. J. Ghimire, A. M. Jones, G. Aivazian, J. Yan, D. G. Mandrus, D. Xiao and W. Yao, *Nat. Commun.*, 2013, **4**, 1474.

80 K. F. Mak, K. He, C. Lee, G. H. Lee, J. Hone, T. F. Heinz and J. Shan, *Nat. Mater.*, 2013, **12**, 207–211.

81 W. Yao, D. Xiao and Q. Niu, *Phys. Rev. B: Condens. Matter Mater. Phys.*, 2008, **77**, 235406.

82 D. H. Kang, M. S. Kim, J. Shim, J. Jeon, H. Y. Park, W. S. Jung, H. Y. Yu, C. H. Pang, S. Lee and J. H. Park, *Adv. Funct. Mater.*, 2015, **25**, 4219–4227.

83 M. Buscema, J. O. Island, D. J. Groenendijk, S. I. Blanter, G. A. Steele, H. S. van der Zant and A. Castellanos-Gomez, *Chem. Soc. Rev.*, 2015, **44**, 3691–3718.

84 K. Novoselov, A. Mishchenko, A. Carvalho and A. C. Neto, *Science*, 2016, **353**, aac9439.

85 A. K. Geim and I. V. Grigorieva, *Nature*, 2013, **499**, 419–425.

86 H. M. Li, D. Lee, D. Qu, X. Liu, J. Ryu, A. Seabaugh and W. J. Yoo, *Nat. Commun.*, 2015, **6**, 6564.

87 J. Y. Lim, A. Pezeshki, S. Oh, J. S. Kim, Y. T. Lee, S. Yu, D. K. Hwang, G. H. Lee, H. J. Choi and S. Im, *Adv. Mater.*, 2017, **29**, 170198.

88 X. Liu, D. Qu, J. Ryu, F. Ahmed, Z. Yang, D. Lee and W. J. Yoo, *Adv. Mater.*, 2016, **28**, 2345–2351.

89 S. Walia, S. Balendhran, Y. Wang, R. Ab Kadir, A. Sabirin Zoolfakar, P. Atkin, J. Zhen Ou, S. Sriram, K. Kalantar-zadeh and M. Bhaskaran, *Appl. Phys. Lett.*, 2013, **103**, 232105.

90 H. Qiu, L. Pan, Z. Yao, J. Li and Y. Shi, *Appl. Phys. Lett.*, 2012, **100**, 123104.

91 S. Das, H. Y. Chen, A. V. Penumatcha and J. Appenzeller, *Nano Lett.*, 2013, **13**, 100–105.

92 C. Gong, C. Huang, J. Miller, L. Cheng, Y. Hao, D. Cobden, J. Kim, R. S. Ruoff, R. M. Wallace and K. Cho, *ACS Nano*, 2013, **7**, 11350–11357.

93 W. Liu, J. Kang, D. Sarkar, Y. Khatami, D. Jena and K. Banerjee, *Nano Lett.*, 2013, **13**, 1983–1990.

94 H. M. Li, D. Y. Lee, M. S. Choi, D. Qu, X. Liu, C. H. Ra and W. J. Yoo, *Sci. Rep.*, 2014, **4**, 4041.

95 W. Mönch, *Appl. Phys. Lett.*, 1998, **72**, 1899–1901.

96 H. Liu, M. Si, S. Najmaei, A. T. Neal, Y. Du, P. M. Ajayan, J. Lou and P. D. Ye, *Nano Lett.*, 2013, **13**, 2640–2646.

3124 | *Chem. Soc. Rev.*, 2018, **47**, 3100–3128

This journal is © The Royal Society of Chemistry 2018

97 H. Liu, M. Si, Y. Deng, A. T. Neal, Y. Du, S. Najmaei, P. M. Ajayan, J. Lou and P. D. Ye, *ACS Nano*, 2013, **8**, 1031–1038.

98 D. Liu, Y. Guo, L. Fang and J. Robertson, *Appl. Phys. Lett.*, 2013, **103**, 183113.

99 C. D. English, G. Shine, V. E. Dorgan, K. C. Saraswat and E. Pop, *Nano Lett.*, 2016, **16**, 3824–3830.

100 D. Somvanshi, S. Kallatt, C. Venkatesh, S. Nair, G. Gupta, J. K. Anthony, D. Karmakar and K. Majumdar, *Phys. Rev. B: Condens. Matter Mater. Phys.*, 2017, **96**, 205423.

101 Y. Liu, J. Guo, Y. Wu, E. Zhu, N. O. Weiss, Q. He, H. Wu, H.-C. Cheng, Y. Xu and I. Shakir, *Nano Lett.*, 2016, **16**, 6337–6342.

102 C. Gong, L. Colombo, R. M. Wallace and K. Cho, *Nano Lett.*, 2014, **14**, 1714–1720.

103 S. Das and J. Appenzeller, *Appl. Phys. Lett.*, 2013, **103**, 103501.

104 J. Kang, W. Liu, D. Sarkar, D. Jena and K. Banerjee, *Phys. Rev. X*, 2014, **4**, 031005.

105 N. Kaushik, A. Nipane, F. Basheer, S. Dubey, S. Grover, M. M. Deshmukh and S. Lodha, *Appl. Phys. Lett.*, 2014, **105**, 113505.

106 K.-K. Liu, W. Zhang, Y.-H. Lee, Y.-C. Lin, M.-T. Chang, C.-Y. Su, C.-S. Chang, H. Li, Y. Shi and H. Zhang, *Nano Lett.*, 2012, **12**, 1538–1544.

107 S. Chuang, C. Battaglia, A. Azcatl, S. McDonnell, J. S. Kang, X. Yin, M. Tosun, R. Kapadia, H. Fang, R. M. Wallace and A. Javey, *Nano Lett.*, 2014, **14**, 1337–1342.

108 M. Tosun, S. Chuang, H. Fang, A. B. Sachid, M. Hettick, Y. Lin, Y. Zeng and A. Javey, *ACS Nano*, 2014, **8**, 4948–4953.

109 M. M. Perera, M.-W. Lin, H.-J. Chuang, B. P. Chamlagain, C. Wang, X. Tan, M. M.-C. Cheng, D. Tománek and Z. Zhou, *ACS Nano*, 2013, **7**, 4449–4458.

110 G. Wang, L. Bao, T. Pei, R. Ma, Y.-Y. Zhang, L. Sun, G. Zhang, H. Yang, J. Li and C. Gu, *Nano Lett.*, 2016, **16**, 6870–6878.

111 K. Geim and K. S. Novoselov, *Nat. Mater.*, 2007, **6**, 183–191.

112 L. Yu, Y.-H. Lee, X. Ling, E. J. Santos, Y. C. Shin, Y. Lin, M. Dubey, E. Kaxiras, J. Kong and H. Wang, *Nano Lett.*, 2014, **14**, 3055–3063.

113 L. Britnell, R. Gorbachev, R. Jalil, B. Belle, F. Schedin, A. Mishchenko, T. Georgiou, M. Katsnelson, L. Eaves and S. Morozov, *Science*, 2012, **335**, 947–950.

114 X. Cui, G. H. Lee, Y. D. Kim, G. Arefe, P. Y. Huang, C. H. Lee, D. A. Chenet, X. Zhang, L. Wang, F. Ye, F. Pizzochero, B. S. Jessen, K. Watanabe, T. Taniguchi, D. A. Muller, T. Low, P. Kim and J. Hone, *Nat. Nanotechnol.*, 2015, **10**, 534–540.

115 T. Roy, M. Tosun, J. S. Kang, A. B. Sachid, S. B. Desai, M. Hettick, C. C. Hu and A. Javey, *ACS Nano*, 2014, **8**, 6259–6264.

116 H.-J. Chuang, X. Tan, N. J. Ghimire, M. M. Perera, B. Chamlagain, M. M.-C. Cheng, J. Yan, D. Mandrus, D. Tománek and Z. Zhou, *Nano Lett.*, 2014, **14**, 3594–3601.

117 Y. Du, L. Yang, J. Zhang, H. Liu, K. Majumdar, P. D. Kirsch and D. Y. Peide, *IEEE Electron Device Lett.*, 2014, **35**, 599–601.

118 J. R. Chen, P. M. Odenthal, A. G. Swartz, G. C. Floyd, H. Wen, K. Y. Luo and R. K. Kawakami, *Nano Lett.*, 2013, **13**, 3106–3110.

119 A. Dankert, L. Langouche, M. V. Kamalakar and S. P. Dash, *ACS Nano*, 2014, **8**, 476–482.

120 V. Heine, *Phys. Rev.*, 1965, **138**, A1689.

121 J. Tersoff, *Phys. Rev. Lett.*, 1984, **52**, 465.

122 R. T. Tung, *Phys. Rev. B: Condens. Matter Mater. Phys.*, 2001, **64**, 205310.

123 S. Lee, A. Tang, S. Aloni and H.-S. P. Wong, *Nano Lett.*, 2016, **16**, 276–281.

124 J. Wang, Q. Yao, C. W. Huang, X. Zou, L. Liao, S. Chen, Z. Fan, K. Zhang, W. Wu and X. Xiao, *Adv. Mater.*, 2016, **28**, 8302–8308.

125 X. Cui, E.-M. Shih, L. A. Jauregui, S. H. Chae, Y. D. Kim, B. Li, D. Seo, K. Pistunova, J. Yin and J.-H. Park, *Nano Lett.*, 2017, **17**, 4781–4786.

126 X. Zou, J. Wang, C. H. Chiu, Y. Wu, X. Xiao, C. Jiang, W. W. Wu, L. Mai, T. Chen and J. Li, *Adv. Mater.*, 2014, **26**, 6255–6261.

127 S. McDonnell, B. Brennan, A. Azcatl, N. Lu, H. Dong, C. Buie, J. Kim, C. L. Hinkle, M. J. Kim and R. M. Wallace, *ACS Nano*, 2013, **7**, 10354–10361.

128 J. Lin, J. Zhong, S. Zhong, H. Li, H. Zhang and W. Chen, *Appl. Phys. Lett.*, 2013, **103**, 063109.

129 S. McDonnell, A. Azcatl, R. Addou, C. Gong, C. Battaglia, S. Chuang, K. Cho, A. Javey and R. M. Wallace, *ACS Nano*, 2014, **8**, 6265–6272.

130 Y. Shi, C. Hamsen, X. Jia, K. K. Kim, A. Reina, M. Hofmann, A. L. Hsu, K. Zhang, H. Li and Z.-Y. Juang, *Nano Lett.*, 2010, **10**, 4134–4139.

131 H.-J. Chuang, B. Chamlagain, M. Koehler, M. M. Perera, J. Yan, D. Mandrus, D. Tománek and Z. Zhou, *Nano Lett.*, 2016, **16**, 1896–1902.

132 A. R. Kim, Y. Kim, J. Nam, H.-S. Chung, D. J. Kim, J.-D. Kwon, S. W. Park, J. Park, S. Y. Choi and B. H. Lee, *Nano Lett.*, 2016, **16**, 1890–1895.

133 Z. Yin, H. Li, H. Li, L. Jiang, Y. Shi, Y. Sun, G. Lu, Q. Zhang, X. Chen and H. Zhang, *ACS Nano*, 2012, **6**, 74–80.

134 X. Li, J. T. Mullen, Z. Jin, K. M. Borysenko, M. B. Nardelli and K. W. Kim, *Phys. Rev. B: Condens. Matter Mater. Phys.*, 2013, **87**, 115418.

135 B. W. Baugher, H. O. Churchill, Y. Yang and P. Jarillo-Herrero, *Nano Lett.*, 2013, **13**, 4212–4216.

136 Z. Yu, Y. Pan, Y. Shen, Z. Wang, Z. Y. Ong, T. Xu, R. Xin, L. Pan, B. Wang, L. Sun, J. Wang, G. Zhang, Y. W. Zhang, Y. Shi and X. Wang, *Nat. Commun.*, 2014, **5**, 5290.

137 Y. Liu, H. Wu, H.-C. Cheng, S. Yang, E. Zhu, Q. He, M. Ding, D. Li, J. Guo and N. O. Weiss, *Nano Lett.*, 2015, **15**, 3030–3034.

138 N. Ma and D. Jena, *Phys. Rev. X*, 2014, **4**, 011043.

139 Z. Yu, Z. Y. Ong, Y. Pan, Y. Cui, R. Xin, Y. Shi, B. Wang, Y. Wu, T. Chen and Y. W. Zhang, *Adv. Mater.*, 2016, **28**, 547–552.

140 B. Radisavljevic and A. Kis, *Nat. Mater.*, 2013, **12**, 815–820.

141 H. Wang, L. Yu, Y. H. Lee, Y. Shi, A. Hsu, M. L. Chin, L. J. Li, M. Dubey, J. Kong and T. Palacios, *Nano Lett.*, 2012, **12**, 4674–4680.

This journal is © The Royal Society of Chemistry 2018

Chem. Soc. Rev., 2018, **47**, 3100–3128 | 3125

142 S. H. H. Shokouh, P. J. Jeon, A. Pezeshki, K. Choi, H. S. Lee, J. S. Kim, E. Y. Park and S. Im, *Adv. Funct. Mater.*, 2015, **25**, 7208–7214.

143 S. Kim, A. Konar, W. S. Hwang, J. H. Lee, J. Lee, J. Yang, C. Jung, H. Kim, J. B. Yoo, J. Y. Choi, Y. W. Jin, S. Y. Lee, D. Jena, W. Choi and K. Kim, *Nat. Commun.*, 2012, **3**, 1011.

144 D. Jena and A. Konar, *Phys. Rev. Lett.*, 2007, **98**, 136805.

145 Z. Yu, Z. Y. Ong, S. Li, J. B. Xu, G. Zhang, Y. W. Zhang, Y. Shi and X. Wang, *Adv. Funct. Mater.*, 2017, **27**, 1604093.

146 Y. Cui, R. Xin, Z. Yu, Y. Pan, Z. Y. Ong, X. Wei, J. Wang, H. Nan, Z. Ni and Y. Wu, *Adv. Mater.*, 2015, **27**, 5230–5234.

147 C. Zhou, X. Wang, S. Raju, Z. Lin, D. Villaroman, B. Huang, H. L.-W. Chan, M. Chan and Y. Chai, *Nanoscale*, 2015, **7**, 8695–8700.

148 S. M. Sze and K. K. Ng, *Physics of Semiconductor devices*, John Wiley & Sons, 2006.

149 A. Punnoose and A. M. Finkel'stein, *Science*, 2005, **310**, 289–291.

150 B. Radisavljevic, M. B. Whitwick and A. Kis, *ACS Nano*, 2011, **5**, 9934–9938.

151 H. S. Song, S. L. Li, L. Gao, Y. Xu, K. Ueno, J. Tang, Y. B. Cheng and K. Tsukagoshi, *Nanoscale*, 2013, **5**, 9666–9670.

152 W. Yang, Q.-Q. Sun, Y. Geng, L. Chen, P. Zhou, S.-J. Ding and D. W. Zhang, *Sci. Rep.*, 2015, **5**, 11921.

153 A. Azcatl, S. McDonnell, S. KC, X. Peng, H. Dong, X. Qin, R. Addou, G. I. Mordi, N. Lu and J. Kim, *Appl. Phys. Lett.*, 2014, **104**, 111601.

154 J. Yang, S. Kim, W. Choi, S. H. Park, Y. Jung, M.-H. Cho and H. Kim, *ACS Appl. Mater. Interfaces*, 2013, **5**, 4739–4744.

155 L. Li, W. Wang, Y. Chai, H. Li, M. Tian and T. Zhai, *Adv. Funct. Mater.*, 2017, **27**, 1701011.

156 M. M. Furchi, D. K. Polyushkin, A. Pospischil and T. Mueller, *Nano Lett.*, 2014, **14**, 6165–6170.

157 C. R. Dean, A. F. Young, I. Meric, C. Lee, L. Wang, S. Sorgenfrei, K. Watanabe, T. Taniguchi, P. Kim and K. L. Shepard, *Nat. Nanotechnol.*, 2010, **5**, 722–726.

158 S. R. Tamalampudi, Y.-Y. Lu, U. R. Kumar, R. Sankar, C.-D. Liao, B. K. Moorthy, C.-H. Cheng, F. C. Chou and Y.-T. Chen, *Nano Lett.*, 2014, **14**, 2800–2806.

159 E. Liu, M. Long, J. Zeng, W. Luo, Y. Wang, Y. Pan, W. Zhou, B. Wang, W. Hu and Z. Ni, *Adv. Funct. Mater.*, 2016, **26**, 1938–1944.

160 L. Wang, I. Meric, P. Huang, Q. Gao, Y. Gao, H. Tran, T. Taniguchi, K. Watanabe, L. Campos and D. Muller, *Science*, 2013, **342**, 614–617.

161 W. Bao, X. Cai, D. Kim, K. Sridhara and M. S. Fuhrer, *Appl. Phys. Lett.*, 2013, **102**, 042104.

162 B. Chamlagain, Q. Li, N. J. Ghimire, H.-J. Chuang, M. M. Perera, H. Tu, Y. Xu, M. Pan, D. Xaio and J. Yan, *ACS Nano*, 2014, **8**, 5079–5088.

163 K. He, N. Kumar, L. Zhao, Z. Wang, K. F. Mak, H. Zhao and J. Shan, *Phys. Rev. Lett.*, 2014, **113**, 026803.

164 M. M. Ugeda, A. J. Bradley, S.-F. Shi, H. Felipe, Y. Zhang, D. Y. Qiu, W. Ruan, S.-K. Mo, Z. Hussain and Z.-X. Shen, *Nat. Mater.*, 2014, **13**, 1091.

165 Y. Lin, X. Ling, L. Yu, S. Huang, A. L. Hsu, Y. H. Lee, J. Kong, M. S. Dresselhaus and T. Palacios, *Nano Lett.*, 2014, **14**, 5569–5576.

166 A. Raja, A. Chaves, J. Yu, G. Arefe, H. M. Hill, A. F. Rigosi, T. C. Berkelbach, P. Nagler, C. Schüller and T. Korn, *Nat. Commun.*, 2017, **8**, 15251.

167 Y. Zhang, J. Ye, Y. Matsuhashi and Y. Iwasa, *Nano Lett.*, 2012, **12**, 1136–1140.

168 H. Shimotani, H. Asanuma, A. Tsukazaki, A. Ohtomo, M. Kawasaki and Y. Iwasa, *Appl. Phys. Lett.*, 2007, **91**, 082106.

169 K. Ueno, S. Nakamura, H. Shimotani, A. Ohtomo, N. Kimura, T. Nojima, H. Aoki, Y. Iwasa and M. Kawasaki, *Nat. Mater.*, 2008, **7**, 855.

170 K. Novoselov, D. Jiang, F. Schedin, T. Booth, V. Khotkevich, S. Morozov and A. Geim, *Proc. Natl. Acad. Sci. U. S. A.*, 2005, **102**, 10451–10453.

171 J. Svensson and E. E. Campbell, *J. Appl. Phys.*, 2011, **110**, 16.

172 D. Braga, I. Gutierrez Lezama, H. Berger and A. F. Morpurgo, *Nano Lett.*, 2012, **12**, 5218–5223.

173 K. Kam and B. Parkinson, *J. Phys. Chem.*, 1982, **86**, 463–467.

174 Y. Zhang, J. Ye, Y. Yomogida, T. Takenobu and Y. Iwasa, *Nano Lett.*, 2013, **13**, 3023–3028.

175 Y. Wang, J. Xiao, H. Zhu, Y. Li, Y. Alsaid, K. Y. Fong, Y. Zhou, S. Wang, W. Shi and Y. Wang, *Nature*, 2017, **550**, 487–491.

176 Y. Li, K.-A. N. Duerloo, K. Wauson and E. J. Reed, *Nat. Commun.*, 2016, **7**, 10671.

177 L. Li, E. O'Farrell, K. Loh, G. Eda, B. Özyilmaz and N. A. Castro, *Nature*, 2016, **529**, 185–189.

178 J. Ye, Y. Zhang, R. Akashi, M. Bahramy, R. Arita and Y. Iwasa, *Science*, 2012, **338**, 1193–1196.

179 J. Lu, O. Zheliuk, I. Leermakers, N. F. Yuan, U. Zeitler, K. T. Law and J. Ye, *Science*, 2015, **350**, 1353–1357.

180 S. Borkar, *IEEE Micro*, 1999, **19**, 23–29.

181 L. B. Kish, *Phys. Lett. A*, 2002, **305**, 144–149.

182 R. K. Cavin, V. V. Zhirnov, J. A. Hutchby and G. I. Bourianoff, *Fluctuation Noise Lett.*, 2005, **5**, C29–C38.

183 S. Salahuddin and S. Datta, *Nano Lett.*, 2008, **8**, 405–410.

184 J. Müller, T. S. Böscke, U. Schröder, S. Mueller, D. Bräuhaus, U. Böttger, L. Frey and T. Mikolajick, *Nano Lett.*, 2012, 12, 4318–4323.

185 C. H. Cheng and A. Chin, *IEEE Electron Device Lett.*, 2014, **35**, 274–276.

186 M. Si, C.-J. Su, C. Jiang, N. J. Conrad, H. Zhou, K. D. Maize, G. Qiu, C.-T. Wu, A. Shakouri and M. A. Alam, *Nat. Nanotechnol.*, 2018, **13**, 24.

187 H. S. Lee, S. W. Min, M. K. Park, Y. T. Lee, P. J. Jeon, J. H. Kim, S. Ryu and S. Im, *Small*, 2012, **8**, 3111–3115.

188 Y. T. Lee, H. Kwon, J. S. Kim, H.-H. Kim, Y. J. Lee, J. A. Lim, Y.-W. Song, Y. Yi, W.-K. Choi and D. K. Hwang, *ACS Nano*, 2015, **9**, 10394–10401.

189 A. Lipatov, P. Sharma, A. Gruverman and A. Sinitskii, *ACS Nano*, 2015, **9**, 8089–8098.

190 X.-W. Zhang, D. Xie, J.-L. Xu, Y.-L. Sun, X. Li, C. Zhang, R.-X. Dai, Y.-F. Zhao, X.-M. Li and X. Li, *IEEE Electron Device Lett.*, 2015, **36**, 784–786.

3126 | *Chem. Soc. Rev.*, 2018, **47**, 3100–3128

This journal is © The Royal Society of Chemistry 2018

191 C. Ko, Y. Lee, Y. Chen, J. Suh, D. Fu, A. Suslu, S. Lee, J. D. Clarkson, H. S. Choe and S. Tongay, *Adv. Mater.*, 2016, **28**, 2923–2930.

192 Y. Zheng, G.-X. Ni, C.-T. Toh, C.-Y. Tan, K. Yao and B. Özyilmaz, *Phys. Rev. Lett.*, 2010, **105**, 166602.

193 R. C. Naber, C. Tanase, P. W. Blom, G. H. Gelinck, A. W. Marsman, F. J. Touwslager, S. Setayesh and D. M. De Leeuw, *Nat. Mater.*, 2005, **4**, 243–248.

194 X. Wang, P. Wang, J. Wang, W. Hu, X. Zhou, N. Guo, H. Huang, S. Sun, H. Shen and T. Lin, *Adv. Mater.*, 2015, **27**, 6575–6581.

195 J. Hong, Z. Hu, M. Probert, K. Li, D. Lv, X. Yang, L. Gu, N. Mao, Q. Feng and L. Xie, *Nat. Commun.*, 2015, **6**, 6293.

196 Y.-C. Lin, T. Björkman, H.-P. Komsa, P.-Y. Teng, C.-H. Yeh, F.-S. Huang, K.-H. Lin, J. Jadczak, Y.-S. Huang and P.-W. Chiu, *Nat. Commun.*, 2015, **6**, 6736.

197 S. Zhang, C.-G. Wang, M.-Y. Li, D. Huang, L.-J. Li, W. Ji and S. Wu, *Phys. Rev. Lett.*, 2017, **119**, 046101.

198 S. Tongay, J. Suh, C. Ataca, W. Fan, A. Luce, J. S. Kang, J. Liu, C. Ko, R. Raghunathanan and J. Zhou, *Sci. Rep.*, 2013, **3**, 2657.

199 A. Srivastava, M. Sidler, A. V. Allain, D. S. Lembke, A. Kis and A. Imamoğlu, *Nat. Nanotechnol.*, 2015, **10**, 491–496.

200 M. Koperski, K. Nogajewski, A. Arora, V. Cherkez, P. Mallet, J.-Y. Veuillen, J. Marcus, P. Kossacki and M. Potemski, *Nat. Nanotechnol.*, 2015, **10**, 503–506.

201 Y.-M. He, G. Clark, J. R. Schaibley, Y. He, M.-C. Chen, Y.-J. Wei, X. Ding, Q. Zhang, W. Yao and X. Xu, *Nat. Nanotechnol.*, 2015, **10**, 503–506.

202 H.-P. Komsa, S. Kurasch, O. Lehtinen, U. Kaiser and A. V. Krasheninnikov, *Phys. Rev. B: Condens. Matter Mater. Phys.*, 2013, **88**, 035301.

203 M. Matsunaga, A. Higuchi, G. He, T. Yamada, P. Krüger, Y. Ochiai, Y. Gong, R. Vajtai, P. M. Ajayan and J. P. Bird, *ACS Nano*, 2016, **10**, 9730–9737.

204 Y. Chen, J. Xi, D. O. Dumcenco, Z. Liu, K. Suenaga, D. Wang, Z. Shuai, Y.-S. Huang and L. Xie, *ACS Nano*, 2013, **7**, 4610–4616.

205 A.-Y. Lu, H. Zhu, J. Xiao, C.-P. Chuu, Y. Han, M.-H. Chiu, C.-C. Cheng, C.-W. Yang, K.-H. Wei and Y. Yang, *Nat. Nanotechnol.*, 2017, **12**, 744–749.

206 J. Zhang, S. Jia, I. Kholmanov, L. Dong, D. Er, W. Chen, H. Guo, Z. Jin, V. B. Shenoy and L. Shi, *ACS Nano*, 2017, **11**, 8192–8198.

207 A. Azcatl, X. Qin, A. Prakash, C. Zhang, L. Cheng, Q. Wang, N. Lu, M. J. Kim, J. Kim and K. Cho, *Nano Lett.*, 2016, **16**, 5437–5443.

208 Z. Zhang, P. Chen, X. Duan, K. Zang, J. Luo and X. Duan, *Science*, 2017, **357**, 788–792.

209 J. Zhu, Z. Wang, H. Yu, N. Li, J. Zhang, J. Meng, M. Liao, J. Zhao, X. Lu and L. Du, *J. Am. Chem. Soc.*, 2017, **139**, 10216–10219.

210 S. Najmaei, Z. Liu, W. Zhou, X. Zou, G. Shi, S. Lei, B. I. Yakobson, J.-C. Idrobo, P. M. Ajayan and J. Lou, *Nat. Mater.*, 2013, **12**, 754–759.

211 Y. Son, M.-Y. Li, C.-C. Cheng, K.-H. Wei, P. Liu, Q. H. Wang, L.-J. Li and M. S. Strano, *Nano Lett.*, 2016, **16**, 3571–3577.

212 R. Kappera, D. Voiry, S. E. Yalcin, B. Branch, G. Gupta, A. D. Mohite and M. Chhowalla, *Nat. Mater.*, 2014, **13**, 1128–1134.

213 S. Song, D. H. Keum, S. Cho, D. Perello, Y. Kim and Y. H. Lee, *Nano Lett.*, 2015, **16**, 188–193.

214 Y. Ma, B. Liu, A. Zhang, L. Chen, M. Fathi, C. Shen, A. N. Abbas, M. Ge, M. Mecklenburg and C. Zhou, *ACS Nano*, 2015, **9**, 7383–7391.

215 B. Lei, Y. Pan, Z. Hu, J. Zhang, D. Xiang, Y. Zheng, R. Guo, C. Han, L. Wang, J. Lu, L. Yang and W. Chen, *ACS Nano*, 2018, **12**, 2070–2077.

216 Z. Wu, W. Zhao, J. Jiang, T. Zheng, Y.-M. You, J. Lu and Z. Ni, *J. Phys. Chem. C*, 2017, **121**, 12294–12299.

217 A. M. Jones, H. Yu, N. J. Ghimire, S. Wu, G. Aivazian, J. S. Ross, B. Zhao, J. Yan, D. G. Mandrus and D. Xiao, *Nat. Nanotechnol.*, 2013, **8**, 634–638.

218 X. Zhang, Q. Liao, S. Liu, Z. Kang, Z. Zhang, J. Du, F. Li, S. Zhang, J. Xiao and B. Liu, *Nat. Commun.*, 2017, **8**, 15881.

219 X. Li, A. A. Puretzky, X. Sang, S. KC, M. Tian, F. Ceballos, M. Mahjouri-Samani, K. Wang, R. R. Unocic and H. Zhao, *Adv. Funct. Mater.*, 2017, **27**, 1603850.

220 P. Yu, J. Lin, L. Sun, Q. L. Le, X. Yu, G. Gao, C. H. Hsu, D. Wu, T. R. Chang and Q. Zeng, *Adv. Mater.*, 2017, **29**, 1603991.

221 A. Nipane, D. Karmakar, N. Kaushik, S. Karande and S. Lodha, *ACS Nano*, 2016, **10**, 2128–2137.

222 S. McDonnell, R. Addou, C. Buie, R. M. Wallace and C. L. Hinkle, *ACS Nano*, 2014, **8**, 2880–2888.

223 M. Yamamoto, S. Nakaharai, K. Ueno and K. Tsukagoshi, *Nano Lett.*, 2016, **16**, 2720–2727.

224 J. Lu, A. Carvalho, X. K. Chan, H. Liu, B. Liu, E. S. Tok, K. P. Loh, A. Castro Neto and C. H. Sow, *Nano Lett.*, 2015, **15**, 3524–3532.

225 H. Nan, Z. Wu, J. Jiang, A. Zafar, Y. You and Z. Ni, *J. Phys. D: Appl. Phys.*, 2017, **50**, 154001.

226 M. Tosun, L. Chan, M. Amani, T. Roy, G. H. Ahn, P. T. Aheri, C. Carraro, J. W. Ager, R. Maboudian and A. Javey, *ACS Nano*, 2016, **10**, 6853–6860.

227 A. Carvalho and A. C. Neto, *Phys. Rev. B: Condens. Matter Mater. Phys.*, 2014, **89**, 081406.

228 M. Yamamoto, S. Dutta, S. Aikawa, S. Nakaharai, K. Wakabayashi, M. S. Fuhrer, K. Ueno and K. Tsukagoshi, *Nano Lett.*, 2015, **15**, 2067–2073.

229 S. Ross and A. Sussman, *J. Phys. Chem.*, 1955, **59**, 889–892.

230 B. Liu, Y. Ma, A. Zhang, L. Chen, A. N. Abbas, Y. Liu, C. Shen, H. Wan and C. Zhou, *ACS Nano*, 2016, **10**, 5153–5160.

231 W. Zhang, J. K. Huang, C. H. Chen, Y. H. Chang, Y. J. Cheng and L. J. Li, *Adv. Mater.*, 2013, **25**, 3456–3461.

232 W. Choi, M. Y. Cho, A. Konar, J. H. Lee, G. B. Cha, S. C. Hong, S. Kim, J. Kim, D. Jena and J. Joo, *Adv. Mater.*, 2012, **24**, 5832–5836.

233 D.-S. Tsai, K.-K. Liu, D.-H. Lien, M.-L. Tsai, C.-F. Kang, C.-A. Lin, L.-J. Li and J.-H. He, *ACS Nano*, 2013, **7**, 3905–3911.

234 D. Kufer and G. Konstantatos, *Nano Lett.*, 2015, **15**, 7307–7313.

This journal is © The Royal Society of Chemistry 2018

Chem. Soc. Rev., 2018, **47**, 3100–3128 | 3127

235 J. Li, M. M. Naiini, S. Vaziri, M. C. Lemme and M. Östling, *Adv. Funct. Mater.*, 2014, **24**, 6524–6531.

236 R. H. Bube, *Photoconductivity of solids*, RE Krieger Pub. Co., 1978.

237 S. Ghatak and A. Ghosh, *Appl. Phys. Lett.*, 2013, **103**, 122103.

238 S. Ghatak, A. N. Pal and A. Ghosh, *ACS Nano*, 2011, **5**, 7707–7712.

239 H. Fang and W. Hu, *Adv. Sci.*, 2017, **4**, 1700323.

240 G. Konstantatos and E. H. Sargent, *Nat. Nanotechnol.*, 2010, **5**, 391–400.

241 Y. H. Chang, W. Zhang, Y. Zhu, Y. Han, J. Pu, J. K. Chang, W. T. Hsu, J. K. Huang, C. L. Hsu, M. H. Chiu, T. Takenobu, H. Li, C. I. Wu, W. H. Chang, A. T. Wee and L. J. Li, *ACS Nano*, 2014, **8**, 8582–8590.

242 Y. Tsai, Z. Chu, Y. Han, C. P. Chuu, D. Wu, A. Johnson, F. Cheng, M. Y. Chou, D. A. Muller and X. Li, *Adv. Mater.*, 2017, **29**, 1703680.

243 H. Wang, C. Zhang, W. Chan, S. Tiwari and F. Rana, *Nat. Commun.*, 2015, **6**, 8831.

244 H. Wang, C. Zhang and F. Rana, *Nano Lett.*, 2014, **15**, 339–345.

245 H. Wang, J. H. Strait, C. Zhang, W. Chan, C. Manolatou, S. Tiwari and F. Rana, *Phys. Rev. B: Condens. Matter Mater. Phys.*, 2015, **91**, 165411.

246 D. Lagarde, L. Bouet, X. Marie, C. Zhu, B. Liu, T. Amand, P. Tan and B. Urbaszek, *Phys. Rev. Lett.*, 2014, **112**, 047401.

247 T. Korn, S. Heydrich, M. Hirmer, J. Schmutzler and C. Schüller, *Appl. Phys. Lett.*, 2011, **99**, 102109.

248 C. J. Docherty, P. Parkinson, H. J. Joyce, M.-H. Chiu, C.-H. Chen, M.-Y. Lee, L.-J. Li, L. M. Herz and M. B. Johnston, *ACS Nano*, 2014, **8**, 11147–11153.

249 J. Shim, A. Oh, D. H. Kang, S. Oh, S. K. Jang, J. Jeon, M. H. Jeon, M. Kim, C. Choi and J. Lee, *Adv. Mat*, 2016, **28**, 6985–6992.

250 V. Klee, E. Preciado, D. Barroso, A. E. Nguyen, C. Lee, K. J. Erickson, M. Triplett, B. Davis, I.-H. Lu and S. Bobek, *Nano Lett.*, 2015, **15**, 2612–2619.

251 J.-G. Song, G. H. Ryu, S. J. Lee, S. Sim, C. W. Lee, T. Choi, H. Jung, Y. Kim, Z. Lee and J.-M. Myoung, *Nat. Commun.*, 2015, **6**, 7817.

252 H. Yamaguchi, R. Kapper, S. Lei., S. Najmaei, B. D. Mangum, G. Gupta, P. M. Ajayan, J. Lou, M. Chhowalla, J. J. Crochet and A. D. Mohite, *ACS Nano*, 2015, **9**, 840–849.

253 D. Jariwala, T. J. Marks and M. C. Hersam, *Nat. Mater.*, 2016, **16**, 171.

254 M. L. Tsai, M. Y. Li, J. R. D. Retamal, K. T. Lam, Y. C. Lin, K. Suenaga, L. J. Chen, G. Liang, L. J. Li and H. He Jr, *Adv. Mater.*, 2017, **29**, 1701168.

255 M.-Y. Li, Y. Shi, C.-C. Cheng, L.-S. Lu, Y.-C. Lin, H.-L. Tang, M.-L. Tsai, C.-W. Chu, K.-H. Wei and J.-H. He, *Science*, 2015, **349**, 524–528.

256 W.-R. Wei, M.-L. Tsai, S.-T. Ho, S.-H. Tai, C.-R. Ho, S.-H. Tsai, C.-W. Liu, R.-J. Chung and J.-H. He, *Nano Lett.*, 2013, **13**, 3658–3663.

257 X. Zhu, N. R. Monahan, Z. Gong, H. Zhu, K. W. Williams and C. A. Nelson, *J. Am. Chem. Soc.*, 2015, **137**, 8313–8320.

258 H. Li, J. Wu, X. Huang, Z. Yin, J. Liu and H. Zhang, *ACS Nano*, 2014, **8**, 6563–6570.

259 C. Palacios-Berraquero, M. Barbone, D. M. Kara, X. Chen, I. Goykhman, D. Yoon, A. K. Ott, J. Beitner, K. Watanabe and T. Taniguchi, *Nat. Commun.*, 2016, **7**, 12978.

260 G. Clark, J. R. Schaibley, J. Ross, T. Taniguchi, K. Watanabe, J. R. Hendrickson, S. Mou, W. Yao and X. Xu, *Nano Lett.*, 2016, **16**, 3944–3948.

261 Y. Rong, Y. Sheng, M. Pacios, X. Wang, Z. He, H. Bhaskaran and J. H. Warner, *ACS Nano*, 2015, **10**, 1093–1100.

3128 | *Chem. Soc. Rev.*, 2018, **47**, 3100–3128

This journal is © The Royal Society of Chemistry 2018